# Energy Coupling and Stoichiometry of $Zn^{2+}/H^{+}$ Antiport by the Cation Diffusion Facilitator YiiP

Adel Hussein[1]*, Shujie Fan[2]*, Maria Lopez-Redondo[1], Ian Kenney[2], Xihui Zhang[1], Oliver Beckstein[§2], David L. Stokes[§1]

[1] Dept. of Cell Biology, NYU School of Medicine, New York, NY 10016 USA

[2] Dept. of Physics, Arizona State University, Tempe AZ

* A. Hussein and S. Fan contributed equally to this paper

[§] O. Beckstein and D.L. Stokes serve as corresponding authors

## ABSTRACT

YiiP is a prokaryotic $Zn^{2+}/H^{+}$ antiporter that serves as a model for the Cation Diffusion Facilitator (CDF) superfamily, members of which are generally responsible for homeostasis of transition metal ions. Previous studies of YiiP as well as related CDF transporters have established a homodimeric architecture and the presence of three distinct $Zn^{2+}$ binding sites named A, B, and C. In this study, we use cryo-EM, microscale thermophoresis and molecular dynamics simulations to address the structural and functional roles of individual sites as well as the interplay between $Zn^{2+}$ binding and protonation. Structural studies indicate that site C in the cytoplasmic domain is primarily responsible for stabilizing the dimer and that site B at the cytoplasmic membrane surface controls the structural transition from an inward facing conformation to an occluded conformation. Binding data show that intramembrane site A, which is directly responsible for transport, has a dramatic pH dependence consistent with coupling to the proton motive force. A comprehensive thermodynamic model encompassing $Zn^{2+}$ binding and protonation states of individual residues indicates a transport stoichiometry of 1 $Zn^{2+}$ to 2-3 $H^{+}$ depending on the external pH. This stoichiometry would be favorable in a physiological context, allowing the cell to use the proton gradient as well as the membrane potential to drive the export of $Zn^{2+}$.

## INTRODUCTION

YiiP is a bacterial $Zn^{2+}/H^{+}$ antiporter and a well characterized representative of the Cation Diffusion Facilitator (CDF) superfamily. Members of this family play important roles in homeostasis of transition metal ions such as $Zn^{2+}$, $Mn^{2+}$, $Co^{2+}$, and $Fe^{2+}$ (Montanini et al., 2007). $Mn^{2+}$ transporters from this superfamily are prevalent in plants, where this metal ion is essential for oxygen generation by photosystem II as well as for a variety of other enzymatic functions (Alejandro et al., 2020). $Zn^{2+}$ CDF transporters are widespread in organisms from all kingdoms of life reflecting a large influence of this ion on cell biology. An estimated 10% of proteins employ $Zn^{2+}$ either as a catalytic co-factor (e.g., carbonic anhydrase and cytochrome C oxidase) or as a structural element (e.g., Zn-finger transcription factors and steroid receptors) (Maret, 2013). In mammals, high concentrations are found in a variety of intracellular vesicles that are key players in the immune system, synaptic transmission, insulin trafficking, and fertilization (Kambe et al., 2015). $Zn^{2+}$ figures in host-pathogen interactions, with the host attempting to either deprive or poison pathogens residing in endosomes (Lonergan and Skaar, 2019). Despite its prevalence, the bulk of intracellular $Zn^{2+}$ is bound to protein, with vanishingly small ($<10^{-12}$ M) concentrations of free $Zn^{2+}$ in the cytoplasm (Liang et al., 2016; Outten and O'Halloran, 2001). Homeostasis is maintained by CDF transporters, which generally export $Zn^{2+}$ from the cytoplasm, as well as members of the Zinc-regulated or Iron-regulated transport Proteins (ZIP), P-type ATPase and ATP-binding cassette (ABC) superfamilies (Yin et al., 2022).

YiiP serves as a model for studying structural and mechanistic properties of CDF transporters. Structures of homologs from both *E. coli* and *S. oneidensis* in different conformational states provide a framework for describing the archetypal alternating access mechanism (Lopez-Redondo et al., 2021; Lopez-Redondo et al., 2018; Lu et al., 2009; Lu and Fu, 2007). Molecular Dynamics has been used to study dynamics (Sala et al., 2019), to define the transport pathway (Sharma and Merz, 2022) and, together with in vitro binding assays, to characterize the $K_d$ and pKa of Zn binding sites. Our understanding of CDF transporters is amplified by recent MD simulations of Znt2 (Golan et al., 2018; Golan et al., 2019), cryo-EM structures of Znt8 (Daniels et al., 2020; Xue et al., 2020; Zhang et al., 2023) and Znt7 (Han et al., 2022), as well as X-ray structures of isolated cytoplasmic domains from a number of different species (Udagedara et al., 2020). Together, these studies establish characteristics of $Zn^{2+}$ binding sites, a conserved homodimeric architecture, and the nature of inward-facing (IF) and outward-facing (OF) states that presumably characterize all CDF transporters.

Despite this extensive work, there is uncertainty about key mechanistic questions that we have sought to address in the current work. Our primary goal was to obtain experimental evidence for the individual roles of the three $Zn^{2+}$ binding sites found on each YiiP protomer (Cotrim et al., 2019). Site A is within the transmembrane domain (TMD) and features three Asp and one His residues; it is alternately exposed to the cytoplasm or to the periplasm in IF and OF states, respectively, and is thus directly responsible for transport of ions across the membrane. Although each molecule composing the dimer appears to have an independent transport pathway, there is unresolved potential for cooperativity. Site C within the C-terminal domain (CTD) is a binuclear site featuring four His and two Asp residues; one of these sites (C1) is well conserved whereas the other (C2) is not (Parsons et al., 2018). Site B is on the loop between transmembrane helices 2 and 3 (TM2-TM3) featuring two His and one Asp residue. Despite a lack of sequence homology for sites B and C2, the structure of Znt8 showed Zn ions at similar locations of the tertiary fold, but bound at different locations in the linear sequence, suggesting that these non-conserved, auxiliary sites may have functional significance (Xue et al., 2020).

Another goal was to address the role of protons in the transport process. There is ample evidence supporting $Zn^{2+}/H^{+}$ antiport. In vitro assays with Znt1, Znt2, ZitB and CzcD showed pH dependence of transport (Chao and Fu, 2004a; Cotrim et al., 2021; Guffanti et al., 2002; Shusterman et al., 2014). Binding studies with Znt8 (Zhang et al., 2023) as well as computational studies with Znt2 (Golan et al., 2019) and YiiP (Sharma and Merz, 2022) showed an interplay between $Zn^{2+}$ and $H^{+}$ binding at site A. However, there are discrepancies in stoichiometry, with work on ZitB (Chao and Fu, 2004a) and YiiP (Chao and Fu, 2004b) supporting a 1:1 exchange of $Zn^{2+}$ and $H^{+}$, whereas studies of CzcD (Guffanti et al., 2002) and Znt2 suggest 1:2 (Golan et al., 2019). There is also recent evidence for $Zn^{2+}/Ca^{2+}$ antiport by Znt1 in neurons (Gottesman et al., 2022).

For the current study, we have generated mutants of YiiP and have used cryo-EM and microscale thermophoresis (MST) to measure the pH dependence and structural effects of $Zn^{2+}$ binding at each of the three sites. In addition, we have used molecular dynamics (MD) simulations together with the experimental MST data to deduce the pKa of residues at these sites and to address the stoichiometry of transport. From these data, we conclude that $Zn^{2+}$ binding at site C is responsible for the integrity of the homodimer. Release of $Zn^{2+}$ from site B triggers a conformational change in which the transport site A becomes occluded, suggesting a potential relay of $Zn^{2+}$ between these two sites. Occlusion of only one protomer breaks the symmetry of the dimer and suggests that the transport process is not cooperative. In addition, binding affinity at site A displays a dramatic pH dependence, which can be explained by the protonation of 2 or 3 of the residues comprising this site. A corresponding $Zn^{2+}/H^{+}$ antiport stoichiometry of 1:2 or 1:3, depending on pH, is consistent with energetic coupling of $Zn^{2+}$ export to the proton-motive force in a physiological setting.

96 # RESULTS

97 ## Mutants used to study the structural effects of $Zn^{2+}$ binding

98 In order to study effects of $Zn^{2+}$ binding at individual sites, we produced mutants of YiiP
99 from *Shewanella oneidensis*. The D51A mutation was introduced to preclude binding at site A
100 and D70A to preclude binding at site B. For site C we mutated Asp287, because it bridges the
101 two $Zn^{2+}$ ions at that site and we anticipated that D287A would therefore eliminate both ions.
102 The wild-type (WT) protein studied in previous work (Coudray et al., 2013; Lopez-Redondo et
103 al., 2021; Lopez-Redondo et al., 2018) served as a positive control. For each of these
104 constructs, protein was expressed in *E. coli*, solubilized in decyl-β-D-maltoside and purified by
105 affinity chromatography. To ensure binding of $Zn^{2+}$ rather than other metal ions picked up during
106 growth and initial purification (e.g., $Ni^{2+}$), we incubated the protein overnight with chelators and
107 then added 250 μM $Zn_2SO_4$ prior to the final purification step. As in previous work (Lopez-
108 Redondo et al., 2021), we used an Fab antibody fragment to produce a larger complex
109 amenable to cryo-EM analysis: 165 kDa comprising the YiiP homodimer (65 kDa) bound to two
110 Fab's (50 kDa each).

111 ## Site A: D51A mutation

112 The structure of the D51A complex was solved at 3.6 Å resolution (Fig. 1b, Suppl. Fig. 1,
113 Table 1) revealing an architecture very similar to untreated, WT YiiP (PDB code 7KZZ) that
114 represents the IF, holo state (Lopez-Redondo et al., 2021). Specifically, YiiP formed a two-fold
115 symmetric homodimer with Fab molecules bound near the C-terminus of each CTD. Density for
116 $Zn^{2+}$ ions is clearly visible at sites B and C (Suppl. Fig. 2e and f). At site A, however, this
117 structure lacked density (Suppl. Fig. 2d), confirming that the D51A mutation effectively
118 eliminated binding at this site.

119 For comparison, we solved the structure from the WT construct that was similarly loaded
120 with $Zn^{2+}$. As expected, this 3.8 Å resolution structure (Fig. 1a, Suppl. Fig. 1) is indistinguishable
121 from 7KZZ, which is also from the WT construct but not treated with chelators or explicitly
122 loaded with $Zn^{2+}$ (RMSD 1.07 Å for all 562 Cα atoms), Despite overall similarity, comparison
123 with the D51A structure showed movements of TM1, TM4 and TM5 (Fig. 2a), which resulted in
124 a notably elevated RMSD for this region: 4.7 Å based on the corresponding 200 Cα atoms
125 compared to 0.69 Å for the 352 residues composing the rest of the YiiP dimer. The cytoplasmic
126 end of TM5 had the largest differences. Specifically, a kink is introduced near His155 and the
127 TM4-TM5 loop is disordered (Suppl. Fig. 2d), suggesting a flexibility of this region in the
128 absence of $Zn^{2+}$ at site A.

129 ## Site B: D70A mutation

130 An initial structure of the D70A construct revealed a global conformational change
131 reminiscent of the previously solved WT, apo state (PDB 7KZX) produced by removal of $Zn^{2+}$
132 with chelators (Lopez-Redondo et al., 2021). The most salient feature of this conformation is a
133 kink between TMD and CTD, which disrupts the overall two-fold symmetry of the complex.
134 During image processing, it became evident that there were in fact multiple conformations in the
135 dataset from D70A, which ultimately generated two distinct structures at 4.0 and 3.9 Å
136 resolution (Fig. 1c, Suppl. Fig. 3). Unlike the WT, apo structure (7KZX), both of these new
137 structures revealed densities at sites A and C (Suppl. Fig. 2g,i,j, and l), consistent with $Zn^{2+}$
138 binding to intact sites. However, the two structures differed both in the conformation of the TMD
139 and in the orientation of the CTD. One of these structures, termed D70A_sym, has a TMD

140 displaying local two-fold symmetry, in which both protomers adopt the IF state (Fig. 2b). Like the
141 WT, apo structure, the TM2/TM3 loops, which harbor Asp70 and site B, are disordered. In the
142 other structure, termed D70A_asym, one TMD adopts the IF state with a disordered TM2/TM3
143 loop, whereas the other TMD adopts a novel conformation in which the TM2/TM3 loop extends
144 ~17 Å away from the membrane to interact with H1 and β1 elements of the CTD from the
145 opposing protomer (Fig. 2c, Suppl. Fig. 5b). In addition to reconfiguring this loop, there are
146 movements in TM1,2,4,5 (Fig. 2d) that close off site A from the cytoplasm. This occlusion is
147 documented by the considerably smaller radius of the cavity leading to this site (Suppl. Fig. 13).

148 Despite these changes, local dimeric elements from the D70A structures superimpose
149 closely onto the corresponding elements from the WT, holo structure. In particular, alignment of
150 CTD's produces low RMSD's of 0.82 Å and 1.08 Å relative to D70A_sym and D70A_asym,
151 respectively (168 Cα atoms). The core helices mediating the TMD dimer interface (TM3/6) also
152 align closely with WT with RMSD's of 0.79 Å and 1.22 Å for D70A_sym and D70A_asym (106
153 Cα atoms, Fig. 2b, d). For D70A_sym, the entire TMD is generally consistent with the WT, holo
154 structure (Fig. 2b), though slight displacement of TM1,4,5 and bending of the cytoplasmic end of
155 TM2 lead to a somewhat elevated RMSD of 2.1 Å for 366 Cα atoms from both protomers after
156 alignment based on TM3/6. For D70A_asym, the TMD in the IF conformation has a similar
157 RMSD of 2.6 Å relative to WT, holo (183 Cα atoms from protomer B, Fig. 2d), whereas the
158 occluded TMD has an elevated RMSD of 5.8 Å (197 Cα atoms from protomer A after aligning
159 TM3/6) due to large differences in the cytoplasmic ends of TM1,2,4,5.

160 The observed structural effects of the D70A mutation are broadly consistent with MD
161 simulations based on the WT structure. In particular, when site B was empty, the TM2/TM3 loop
162 exhibited greatly increased mobility documented by >2-fold increase in root mean square
163 fluctuations (RMSF, Fig. 3a); this result is consistent with disorder of this loop in D70A cryo-EM
164 structures. The CTD also exhibited increased mobility as documented both by the broader
165 distribution of the angles relative to the TMD (Fig. 3d) and by per residue RMSF, in particular
166 when the TMD was used as reference for alignment (Fig. 3b), indicating that the CTD moved as
167 a fairly rigid body relative to the TMD. In structures with $Zn^{2+}$ bound at site B, the TM2/TM3 loop
168 from one protomer is close to the linker between TM6 and the CTD of the opposing protomer
169 (Fig. 3e,f, Suppl. Fig. 2b,e, and n). We therefore used the distance between Cα atoms of Asp72
170 in the TM2/TM3 loop and Arg210 in the TM6/CTD linker from the opposing chain as a collective
171 variable for tracking CTD movement. The corresponding distance distributions (Fig. 3c) are
172 broader and extend to larger values when site B is empty. In simulations of the D72A mutant
173 with $Zn^{2+}$ bound at site B there is a marked increase in CTD/TMD angle (Fig. 4d) as well as a
174 more modest increase in the distance distribution (Fig. 4c). These results, together with
175 structures of D70A_sym and WT, apo, suggest that a salt bridge between Asp72-Arg210 helps
176 maintain the symmetry seen in the holo state. Release of $Zn^{2+}$ from site B causes disordering of
177 the TM2/TM3 loops leading to loss of the salt bridge and thus greater mobility of the CTD.
178 However, the D70A_asym structure indicates that this disordering is transient, as the loop
179 adopts the extended conformation and associates with different elements of the CTD (Fig. 2c).
180 Interestingly, this novel change in the TM2/TM3 loop is coupled with movements of TM1,2,4,5
181 that close site A off from the cytoplasm (Fig. 3i-j, Suppl. Fig. 13). Mapping of electrostatic
182 charge shows that whereas the access channel to site A in the IF protomer is negatively
183 charged, positive charge dominates the cytoplasmic surface of the protomer in the occluded
184 conformation (Fig. 3k,l).

185 ## Site C: D287A and D287A/H263A mutations

186 The D287A mutant was chosen to disrupt site C since it coordinates both $Zn^{2+}$ ions at
187 this site. However, the corresponding structure (3.7 Å resolution, Fig 1d, Suppl. Fig. 4) shows no
188 structural changes relative to the WT structure (1.18 Ä RMSD for all 562 Cα atoms) and $Zn^{2+}$-
189 related densities are still clearly visible at site C (Suppl. Fig. 2o). We therefore introduced a
190 second mutation, D287A/H263A, and the corresponding particles had an unusual appearance
191 consistent with formation of higher order oligomers (Suppl. Fig. 4b). This observation suggested
192 that site C may be responsible for the integrity of the homodimer. Indeed, SEC elution profiles of
193 the YiiP-Fab complex show that the main peak from D287A/H263A is shifted relative to the
194 other mutants (from 11.1 to 10.1 ml, c.f., Suppl. Figs. 1a,b, 3a, 4a,b). Elution profiles from
195 complexes formed with D70A and D287A also have an earlier peak at ~10 ml and, in both
196 cases, image processing revealed a relatively small subpopulation of particles forming a dimer
197 of dimers (Suppl. Fig. 3c & 4e). However, for D287A/H263A, this dimer of dimers represents the
198 main peak and the only class of particles that could be refined to high resolution (3.5 Å) (Suppl.
199 Fig. 4h). For D287A/H263A, higher order oligomers are apparent during 2D and 3D
200 classification (Suppl. Fig. 4d & f) and are likely to explain the earlier elution peak at 8-9 ml.

201 The dimer of dimers from D287A/H263A is stabilized by an unprecedented domain swap
202 in which CTD's and TMD's affiliate with different protomers (Fig. 2g). This domain swap is
203 enabled by a structural transition of the linker between the TMD and the CTD. In particular, the
204 normally unstructured loop between TM6 and the first helix of the CTD (H1) is reconfigured into
205 a very long, continuous α-helix extending from the N-terminus of M6 (Trp178) to the C-terminus
206 of H1 (Glu226). Site C itself is completely disordered and the CTD's are splayed apart (Figs. 2g
207 & Suppl. Fig. 5c): i.e., the distance between Cα atoms of Arg237 and Glu281 is 22.7 Å
208 compared to ~12 Å in structures with an intact site C (Lopez-Redondo et al., 2021). This domain
209 swap was not observed in the dimer-of-dimers formed by D70A and D287A, where the CTD and
210 site C were unperturbed and Fab molecules were uniquely responsible for inter-dimer
211 interactions. Although it was not possible to refine a structure from the higher-order oligomers
212 from D287A/H263A, due to heterogeneity and preferred orientation, they appeared to comprise
213 a linear chain of molecules propagated via this domain swap. These surprising changes in the
214 CTD indicate that site C is indeed crucial in maintaining the integrity of the native homo-dimer.
215 Despite the domain swap, however, TMD's from the D287A/H263A complex are quite congruent
216 with the WT structure (RMSD 1.35 Å for 346 Cα atoms excluding the TM2/TM3 loop) and
217 density for $Zn^{2+}$ ions is clearly visible at site A (Suppl. Fig. 2p). Weak density is visible for the
218 TM2/TM3 loops, indicating that they adopt an extended configuration that disrupts site B and
219 allows them to interact with the CTD; it does not appear that $Zn^{2+}$ is bound at site B in this
220 domain-swapped complex (Suppl. Figs. 2q and 5c,d).

221 ## $Zn^{2+}$ binding affinity

222 To assess the binding affinity of individual $Zn^{2+}$ binding sites, we used MST to analyze a
223 series of mutants designed to isolate the individual sites (Fig. 4 and Suppl. Fig. 6). Specifically,
224 the triple mutant D70A/D287A/H263A was used to study site A, D51A/D287A/H263A to study
225 site B, and D51A/D70A to study site C. To maintain accurate and reproducible $Zn^{2+}$
226 concentrations ranging from nanomolar to micromolar, we used nitrilotriacetic acid (NTA, $K_d$ =
227 14 nM) to buffer $Zn^{2+}$ for sites with high affinity, and citrate ($K_d$ = 12 μM) for sites with lower
228 affinity. At pH 7, sites A and C displayed relatively high affinity ($K_d$ = 16 and 33 nM, respectively,
229 Table 2, Fig. 4), whereas site B had considerably lower affinity ($K_d$ = 1.2 μM). Site C is

230 binuclear, and the apparent affinity was reduced when further mutations were introduced to
231 isolate individual C1 (D51A/D70A/H263A with $K_d$ = 153 nM) and C2 (D51A/D70A/H234A with $K_d$
232 = 223 nM) sites, suggesting cooperative binding of ions at C1 and C2 as implied by the
233 coordination geometry of this site (Fig. 1d inset).

234 To explore the basis for coupling of $Zn^{2+}$ transport to the proton-motive force, we
235 measured $Zn^{2+}$ binding affinity at pH values from 5.6 - 7.4. We found that affinity at site A
236 changed by five orders of magnitude: $K_d$ ranging from 1 nM at pH 7.4 - consistent with the
237 cytosol - to 302 μM at pH 5.6 (Fig. 4a, Table 2). Site B had only modest pH dependence ranging
238 from 1-16.6 μM, whereas Site C changed by two orders of magnitude from 0.033 - 6.7 μM.
239 Cooperativity at site C is consistent with a high Hill coefficient at pH 7 (n=2.9), which fell below 1
240 at lower pH's. However, Hill coefficients obtained for other sites were quite variable (Table 3),
241 including those for sites C1 and C2, making conclusions about cooperativity inconclusive.

242 The domain swap seen in cryo-EM structures of D287A/H263A raises concern that site
243 C mutations might affect affinity measured at other sites. However, in the absence of Fab, all of
244 the mutants used for MST studies eluted from SEC columns at the same volume as WT (Suppl.
245 Fig. 6a-d) indicating that they all adopted the native dimeric structure. This observation suggests
246 that the domain-swapping seen in the structure of D287A/H263A was induced by the Fab
247 molecules. This conclusion is supported by direct comparison of preparations with site C
248 mutations before and after addition of Fab (Suppl. Fig. 6 h & i). In the absence of Fab, they both
249 elute from SEC as a single peak at the expected volume of 12 ml. In the presence of Fab, there
250 is a shift of the main peak consistent with formation of a higher molecular weight complex and,
251 additionally, appearance of a second peak. In the case of D287A-Fab, the main peak at 11.1 ml
252 is consistent with the YiiP-Fab complex seen for the other mutants (Suppl. Fig. 1 & 3) and the
253 second peak at 9.9 ml is consistent with the dimer of native homodimers seen during image
254 processing. In the case of D287A/H263A, the main peak in the presence of Fab is at 10.1 ml
255 and thus consistent with a dimer of domain-swapped dimers and the secondary peak at 8.6 ml
256 is consistent with higher order oligomers seen during cryo-EM processing (Suppl. Fig. 4). In
257 addition, we performed MST analysis with the D70A/D287A mutation as an alternative for
258 measuring affinity at site A. The cryo-EM structure of D287A shows that the native homodimeric
259 assembly is retained and although $Zn^{2+}$ was observed at site C, we expect it will bind at lower
260 affinity and thus not overlap with higher affinity binding at site A. Indeed, this construct produced
261 Kd= ~1 nM at pH 7 and ~6 μM at pH 6, which is consistent with results from
262 D70A/D287A/H263A (Table 2), thus confirming the pH dependence of site A.

263 We also used MD simulations in conjunction with the experimental MST data to address
264 pH dependence of $Zn^{2+}$ binding and to evaluate the contribution of individual residues. To start,
265 we estimated pKa values for each titratable residue at site A (Asp47, Asp51, His155 and
266 Asp159) and site B (Asp70, His73 and His 77) using constant pH MD (CpHMD) simulations with
267 pH replica exchange (Huang et al., 2021) in the absence of $Zn^{2+}$. It was not possible obtain data
268 for site C because the $Zn^{2+}$-free CTD proved unstable in CpHMD simulations. These simulations
269 generated probabilities for each protonation state as a function of pH; these probabilities were fit
270 with the Hill-Langmuir equation to derive per-residue $pK_a$'s (Suppl. Figs. 7-9, Table 4). For site A
271 residues, His155 had the highest predicted $pK_a$ (8.0), followed by Asp159 (4.9), Asp47 (3.8) and
272 Asp51 (2.9). Predicted populations of the individual microstates (s0-s15, Suppl. Figs. 10a & b)
273 indicated that two residues are likely protonated at pH 5.5 with His155 getting protonated first
274 followed by Asp159. Although these simulations were conducted with the IF conformation, we

275 do not expect significant differences for the OF state, given the similarity of site A seen in the X-
276 ray structure (Lu et al., 2009) of the OF state (RMSD of 0.49 Å for 17 Cα atoms on TM2 and
277 TM5 and 1.01 Å for all atoms composing the four residues that coordinate the $Zn^{2+}$ ion). For site
278 B, His73 and His77 have almost identical $pK_a$'s of 8.1, and the dominant state at neutral pH
279 consists of both His73 and His77 protonated (Suppl. Figs. 11a & b).

280 We went on to use a thermodynamic model incorporating both protonated and $Zn^{2+}$-
281 bound states to assess the stoichiometry of transport (Fig. 4h). We used this model to generate
282 $Zn^{2+}$ binding curves based on $pK_a$'s of individual residues and binding free energies for $Zn^2$
283 derived from the experimental MST data (Table 2). Initially, $pK_a$'s of each residue in the absence
284 of $Zn^{2+}$ were taken from the Hill-Langmuir fits to the CpHMD data (Table 4, Suppl. Fig. 9).
285 However, this CpHMD-based model did not agree with the experimental data (Figs. 4d & e),
286 likely due to inaccuracy in microstate $pK_a$ values. We therefore employed a novel modeling
287 method based on the inverse *Multibind* approach (see Methods) to iteratively refine the CpHMD
288 $pK_a$'s and the MST $Zn^{2+}$ binding free energies using the MST data points as a target for Monte
289 Carlo (MC) minimization. This analysis, referred to henceforth as *MST inference*, allowed us to
290 estimate probabilities of all the microstates as a function of pH and $Zn^{2+}$ concentration (Suppl.
291 Figs. 10 & 11). After refinement of parameters by MST inference, the predicted $Zn^{2+}$ binding
292 curves closely reproduced the observed pH-dependence of $Zn^{2+}$ binding at both sites A and B
293 (Figs. 4f & g). The dramatically improved agreement is a consequence of substantial changes in
294 the $pK_a$'s of individual residues based on the MST inference algorithm (Table 4).

295 A more detailed look at the population of microstates predicted by MST inference allows
296 us to explore the interplay of $Zn^{2+}$ and $H^+$ binding under physiological conditions. For site A in
297 the absence of $Zn^{2+}$, the dominant state at cytosolic pH of 7.5 consists of 2 protons bound by
298 His155 and Asp159 (Suppl. Figs. 10c & d). Based on the microscopic $pK_a$ values, we calculated
299 the "coupling energy" (Ullmann, 2003) and thus deduced that these two residues form a coupled
300 system (see Methods). As a result, protonation of His155 and Asp159 is highly cooperative and
301 produces a very steep binding curve (Suppl. Fig. 10e); the singly protonated state is strongly
302 suppressed and the effective $pK_a$ is 7.8 for both residues (Suppl. Fig 10d). At the lower pH of
303 the periplasm, a third proton is recruited by Asp51, whose $pK_a$ increased to 6.5 during
304 refinement by MST inference (Table 4). Regardless of the pH, as $Zn^{2+}$ binds at site A, all the
305 residues are deprotonated (Suppl. Fig. 10f), supporting the idea that $Zn^{2+}$ transport can be
306 coupled with a proton gradient across the plasma membrane. For site B, the dominant state at
307 cytosolic pH in the absence of $Zn^{2+}$ has one protonated residue: either His73 or His77 (Suppl.
308 Fig. 11c & d). Although the microstate $pK_a$'s are equivalent, these site B residues behave quite
309 differently from Site A residues and generate an anti-cooperative binding curve with effective
310 $pK_a$'s of 5.6 and 12.4 (Suppl. Figs. 11e & f). $Zn^{2+}$ binding at cytosolic pH displaces all protons
311 (Suppl. Fig. 11g). Even though protons may co-exist with $Zn^{2+}$ at lower pH's, this is not a
312 physiologically relevant condition given that site B is uniquely exposed to the cytoplasm.

313

314 ## DISCUSSION

315 In this study, we have focused on the properties of individual $Zn^{2+}$ binding sites of YiiP
316 from *S. oneidensis*. Previous studies have shown that this protein forms a homodimer in the IF
317 state with $Zn^{2+}$ ions constitutively bound at three sites (Lopez-Redondo et al., 2018). Treatment
318 with EDTA to remove $Zn^{2+}$ from all three sites induced a conformational change to produce an
319 occluded state, a necessary precursor to the OF state (Lopez-Redondo et al., 2021). For the
320 current work, we generated mutations at each site to measure their binding affinities and to
321 assess their respective roles in generating conformational change. We found that site A,
322 considered to be the transport site in the middle of the TMD, has nanomolar affinity at a
323 cytoplasmic pH of 7.4, which is reduced $10^5$-fold at the more acidic pH of 5.6. Release of $Zn^{2+}$
324 from site A induces only modest movement of the peripheral transmembrane helices, but has no
325 global effect on the architecture of the homodimer. Site B, on the short loop between TM2 and
326 TM3, has much lower affinity in the micromolar range with relatively little pH dependence. When
327 site B lacks $Zn^{2+}$, the loop becomes disordered and the protein undergoes a global
328 conformational change leading to an occluded conformation in one of the protomers. Site C, a
329 binuclear site in the CTD that engages residues from both protomers, has relatively high affinity
330 and intermediate pH dependence. When site C was fully disrupted with a double mutation, the
331 homodimer became destabilized such that the Fab molecules used for cryo-EM imaging
332 induced a domain swap of the CTD leading to higher order oligomers.

333 ### Elements stabilizing the homodimer

334 Dimerization appears to be a universal feature of Cation Diffusion Facilitators. All
335 structures so far show similar elements contributing to a common dimer interface (Suppl. Fig.
336 12). In particular, a conserved salt bridge exists at the cytoplasmic surface of the membrane
337 (Lys79-Asp209 for soYiiP); the cytoplasmic end of the CTD generally includes one or more $Zn^{2+}$
338 sites, and extensive hydrophobic interactions involving TM3 helices mediate TMD interactions
339 (Lopez-Redondo et al., 2021). In early work, the salt bridge was proposed to act as a fulcrum for
340 alternating, scissor-like movements in TMD and CTD driven by relay of $Zn^{2+}$ between sites A
341 and C (Lu et al., 2009). Furthermore, the original X-ray structure of ecYiiP featured a V-shaped
342 architecture in which TMD's were completely disengaged (Lu et al., 2009; Lu and Fu, 2007).
343 However, subsequent work showed that stabilization of TMD interactions by cysteine
344 crosslinking did not inhibit transport activity (Lopez-Redondo et al., 2018) and compact dimeric
345 TMD interfaces were observed in cryo-EM structures of soYiiP, Znt8 and Znt7 (Han et al., 2022;
346 Lopez-Redondo et al., 2018; Xue et al., 2020). Indeed, the TMD interface is a remarkably
347 conserved feature in our new structures of D70A and D287A/H263A mutants, despite large-
348 scale conformational changes involving the TM2/TM3 loop and domain swapping of the CTD.
349 We therefore conclude it to be unlikely that the TMD's undergo large-scale scissoring
350 movements as part of the transport cycle.

351 For isolated CTD's, metal ion dependent scissor-like movements have been well
352 documented using truncated constructs from a variety of species (Cherezov et al., 2008;
353 Udagedara et al., 2020; Zeytuni et al., 2014). We observed similar movements in full-length
354 soYiiP: i.e., the CTD's move apart when $Zn^{2+}$ is removed from site C either by chelation or
355 mutation. However, other elements must contribute, given that isolated CTD's dimerize even in
356 the absence of metal ions and $Zn^{2+}$ ions were not observed at all in the CTD of Znt7 (Han et al.,
357 2022). Nevertheless, the Fab-induced domain swap seen in D287A/H263A indicates that, for
358 soYiiP, CTD interactions are weakened in the absence of $Zn^{2+}$. Conversely, it seems likely that

359 dimer stabilization, via TMD and salt-bridge interactions, lead to enhanced $Zn^{2+}$ binding in the
360 CTD, as evidenced by the considerably higher $Zn^{2+}$ affinity at site C of full-length soYiiP ($K_d$ of
361 33 nM at pH 7) compared to those measured from isolated CTD's ($K_d$ in micromolar range
362 (Udagedara et al., 2020; Zeytuni et al., 2014)). In any case, the relatively high affinity of site C at
363 pH 7 suggests that this site will remain occupied and will serve to ensure dimer stability under
364 physiological conditions.

365 ## Role of the site B

366 Structural effects of the D70A mutation support our previous hypothesis that site B is
367 responsible for inducing a global conformational change. The most conspicuous change is the
368 kink between TMD and CTD, which breaks the global two-fold symmetry of structures that retain
369 $Zn^{2+}$ binding at site B, in which local two-fold axes of CTD and TMD are aligned (Suppl. Fig. 12).
370 Although stable, kinked conformations were not achieved over the time-scale of MD simulations,
371 increased movement of the CTD relative to the TMD is seen both in the previously reported apo
372 state simulations (Lopez-Redondo et al., 2021) and with an empty site B (Fig. 3), indicating a
373 role of the $Zn^{2+}$-bound TM2/TM3 loop in stabilizing the position of the CTD. Indeed, van der
374 Waals interactions are observed between the structured loop from one protomer and the TM6-
375 CTD linker of the opposing protomer on both sides of the dimer (Fig. 3e,f), and MD simulations
376 indicate that a salt bridge between Asp72 and Arg210 may reinforce these interactions (Fig. 3d,
377 c.f., site B in Suppl. Fig. 2).

378 Both cryo-EM structures and MD simulations show that the TM2/TM3 loop becomes
379 disordered when $Zn^{2+}$ is released from site B and this is a likely explanation for increased
380 mobility of the CTD. Two structures were obtained from the D70A mutation in which the CTD
381 becomes progressively more tilted and twisted. In one structure, the TMD's are symmetrical and
382 retain the IF conformation (D70A_sym), whereas in the other structure with more extreme CTD
383 movement (D70A_asym), the TMD transitions to an occluded state. We speculate that these
384 structures represent a sequence of conformational change leading to the occluded state.
385 Although both TM2/TM3 loops are disordered in the D70A_sym structure, one of these loops
386 reforms into an extended conformation in the occluded protomer of the D70A_asym structure
387 (Suppl. Fig. 5). This change results in a novel interaction between the loop and the CTD, which
388 may drive the displacement and bending of membrane helices thus leading to occlusion of the
389 transport site A (Suppl. Fig. 13). This interaction would also prevent the TM2/TM3 loop from
390 rebinding $Zn^{2+}$ until the protein returned to the IF state. On the other side of the dimer, the CTD
391 has lost contact with the TMD, allowing the TM2/TM3 loop to remain disordered and the TMD to
392 remain in the IF state. Interestingly, the TM2/TM3 loops are also extended in the D287A/H263A
393 domain-swapped structure (Suppl. Fig. 5), but in this case, the interactions of this loop with the
394 reconfigured CTD's are quite different and the TMD's remain in the IF state, indicating that a
395 specific structural constraint is required to instigate occlusion.

396 Occlusion of the transport site A is a result of bending of TM5 and tilting of TM1 and 4,
397 thus narrowing the gap between these helices and closing off access to the cytosol. These
398 movements also generate a dramatic difference in the electrostatic surface at the cytoplasmic
399 side of the TMD. In the IF state, the open cavity leading toward site A is negatively charged, as
400 also shown for Znt7 (Han et al., 2022), thus serving to attract $Zn^{2+}$ toward this site. After
401 transition to the occluded state, not only is the cavity closed (Suppl. Fig. 13), but the surface
402 becomes positively charged thus repelling $Zn^{2+}$ (Fig. 3k,l). Previous work has identified a
403 "hydrophobic gate" consisting of two residues at the cytoplasmic ends of TM5 and TM6: Leu154

404 and Leu199 in soYiiP (Gupta et al., 2014). Our previous comparison of holo and apo states
405 showed that these two residues do come closer together in the occluded state (Lopez-Redondo
406 et al., 2021) and homologous residues in Znt7 are close in the OF state and separated in the IF
407 state (Han et al., 2022). Interaction of Leu154 and Leu199 is also seen in the occluded protomer
408 in the D70A_asym structure (Fig. 2d), but these residues are at the periphery of the cavity
409 leading to site A. This observation suggests that interaction of these residues may play an
410 important role in stabilizing the occluded state, but that bending at the cytoplasmic end of TM5
411 (Val148-Ala151) and tilting of TM1 and TM4 may be more directly responsible for blocking
412 access to the transport site.

413 For soYiiP, the IF state appears to be a low-energy, ground state when $Zn^{2+}$ is present at
414 all three sites. Indeed, the IF state has been seen for WT protein both in lipid-based helical
415 crystals (Lopez-Redondo et al., 2018 ) and detergent micelles (Lopez-Redondo et al., 2021), as
416 well as in D287A and D287A/H263A mutant structures, all with RMSD's <1.5 Å. Removal of
417 $Zn^{2+}$ from site B can be viewed as a source of energy for inducing conformational change and
418 likely leading to transport. Interestingly, the occlusion only occurs in one protomer, suggesting a
419 lack of synchrony across the dimer axis. A mixture of conformational states was also observed
420 for Znt8, in which one protomer adopted the OF state while the other was in the IF state. These
421 observations imply that a given protomer may be able to undergo transport while the other
422 remains inactive, as illustrated in Fig. 5.

423 The proposed sequence of conformational change is consistent with the notion that $Zn^{2+}$
424 is initially recruited to site B and that transfer to site A would act as a trigger for the first step of
425 the transport cycle. Such a two-step mechanism might be necessary if $Zn^{2+}$ were delivered to
426 YiiP as a chelate – e.g., with metallothionein or glutathione – that would not have direct access
427 to site A. In the case of $Cu^{+}$, metallochaperones are thought to play a role in delivery (Robinson
428 and Winge, 2010), but so far there is very limited evidence for $Zn^{2+}$ metallochaperones
429 (Chandrangsu et al., 2019). Nevertheless, essentially all of the $Zn^{2+}$ in the cytoplasm exists in
430 chelated form with vanishingly small concentrations of free $Zn^{2+}$ available for direct binding
431 (Choi and Koh, 1998; Outten and O'Halloran, 2001). The accessibility of site B makes it a
432 plausible acceptor as an initial recruitment site. We postulate that site B would only be available
433 for binding $Zn^{2+}$ in the IF apo state (Fig. 5d). Once bound, two features would facilitate transfer
434 to site A: the drastic difference in affinity between sites A and B would generate a large free-
435 energy gradient and the negative charge of the cavity leading to site A, which lies almost directly
436 below site B in the WT, holo structures, would direct the ion toward the transport site. Although
437 the amino acid sequence of site B is not conserved amongst CDF transporters, a $Zn^{2+}$ ion was
438 observed in an analogous juxtamembrane position on Znt8 (Xue et al., 2020) and many CDF
439 transporters have histidine-rich loops, typically between TM4 and TM5, which might fulfill a
440 similar role in recruiting $Zn^{2+}$ and orchestrating conformational change. Indeed, for Znt7 this His-
441 rich loop was shown to bind two $Zn^{2+}$ ions leading these authors also to speculate that it plays a
442 role in recruitment and shuttling to the transport site (Han et al., 2022).

443 ## Stoichiometry of transport and energy coupling

444 The proton-motive force is generally postulated to drive the antiport mechanism utilized
445 by CDF transporters. In the case of YiiP, this antiport involves exchange of $Zn^{2+}$ from the
446 cytoplasm for $H^{+}$ in the periplasm and the stoichiometry of this process is key to energy
447 coupling. In previous work, the $Zn^{2+}$:stoichiometry has been measured to be 1:1 for ZitB (Chao
448 and Fu, 2004a) and deduced by cellular or computational studies to be 1:2 for CzcD (Guffanti et

al., 2002) and Znt2 (Golan et al., 2019), respectively. In addition, isothermal calorimetry was used to deduce a binding stoichiometry for $Cd^{2+}$ of 1:1 for ecYiiP (Chao and Fu, 2004b). For the current work, we refined CpHMD simulation data with experimental MST data using the inverse *Multibind* approach (Kenney and Beckstein, 2023) to infer the prevalent protonation states for site A and thus to address stoichiometry. Our analysis is consistent with $Zn^{2+}$ binding to a fully unprotonated site A regardless of the pH. After $Zn^{2+}$ release, the transport site becomes either doubly or triply protonated, depending on the pH. Due to strong coupling between His155 and Asp159, the singly protonated state is essentially not seen. Thus, this model is consistent with a stoichiometry of at least 1:2, possibly 1:3 in more acidic environments (pH < 6).

Our analysis predicts significant shifts in p$K_a$ for Zn-binding residues. Such shifts reflect strong Coulomb interactions due to both the low dielectric of the membrane and the clustering of several titratable residues at the binding site. Effects of the membrane environment have been studied both by experimental (Gayen et al., 2016; Isom et al., 2010; Morrison et al., 2015) and computational (Henderson et al., 2020; Panahi and Brooks, 2015) methods, showing p$K_a$ values up to 9 for acidic residues. Coupling between nearby residues has also been shown to shift p$K_a$ values (Yue et al., 2017), with estimated p$K_a$ values of 3 and 11 for a di-aspartyl pH sensor in a pH-sensitive calcium channel serving as a dramatic example (Chang et al., 2014). Together with the current work, these examples illustrate the importance of tuning the local environment to harness the energy of the proton motive force.

The $Zn^{2+}$:$H^+$ stoichiometry has crucial physiological consequences for the energetics of transport, which are governed by the Nernst equation describing electrochemical potential. The overall transport cycle can be described as

$$mH_o + nZn_i \rightleftharpoons mH_i + nZn_o$$

with the free energy calculated as

$$\Delta G = RT\ln\frac{[H_i]^m}{[H_o]^m} + RT\ln\frac{[Zn_o]^n}{[Zn_i]^n} + zFV_m$$

where *m* is the number of protons, *n* is the number of $Zn^{2+}$ ions, *z* is the net charge for the reaction and $V_m$ is the membrane potential. Based on this equation, the higher stoichiometries of 1:2 or 1:3 provide the cell with increased leverage over $Zn^{2+}$ transport. In the absence of membrane potential, for example, a 10-fold proton gradient (ΔpH of 1) can produce $Zn^{2+}$ gradients at equilibrium of up to $10^2$ or $10^3$, respectively, instead of simply 10 for a 1:1 stoichiometry (more generally, $10^{m/n}$). Membrane potential represents an important component of the proton motive force that will influence electrogenic transport, where *z* is non-zero. In particular, a stoichiometry of 1:1 would produce net positive charge transfer out of the cell and thus would require working against this membrane potential. Given a potential of -80 mV, relatively normal in *E. coli* (Felle et al., 1980), a 1:1 stoichiometry would produce an unfavorable energy term that would overcome a chemical gradient of one pH unit. In contrast, a 1:2 stoichiometry would be electroneutral and would therefore be unaffected by membrane potential thus generating a $Zn^{2+}$ gradient of $10^2$ as described above. Finally, a stoichiometry of 1:3 would benefit both from the membrane potential as well as from the increased number of protons to theoretically generate a gradient of $10^{4.4}$.

These calculations are based on equilibrium thermodynamics, but the pH dependence of $Zn^{2+}$ binding also has implications for the kinetics of transport. In particular, the dramatic

difference in $K_d$ at cytoplasmic pH of 7.4 (1 nM) compared to more acidic pH's in the periplasm (e.g., 6 μM at pH 6) implies that the on-rate of $Zn^{2+}$ is dominant in the cytoplasm but that the off-rate is enhanced in the periplasm, assuming that the binding site in the OF state has similar pH dependence. This assumption seems plausible given the similarity of transport site geometry of YiiP in the OF state (Lu et al., 2009). Thus, although the final equilibrium concentrations of $Zn^{2+}$ are not affected by the pH dependence of the transport site, the rate of transport and the rate of equilibration will be greatly enhanced (Tanford, 1983).

YiiP has three aspartates and one histidine at site A, whereas many CDF transporters including the mammalian Znt's substitute Asp47 for a second histidine. Previous work has focused on changes in ion specificity associated with this change (Hoch et al., 2012), but it also seems likely to affect stoichiometry. At a minimum, two histidines would make the 1:2 stoichiometry almost certain and a 1:3 stoichiometry highly plausible. The resulting electrogenicity could be desirable for eukaryotic cells in which these transporters operate predominantly in intracellular organelles such as insulin secreting granules, synaptosomes, golgi or zinc-o-somes that are responsible for the dramatic $Zn^{2+}$ sparks during oocyte fertilization (Chu, 2018; Hara et al., 2017). Since the pH gradient of these organelles is modest, additional driving force from the membrane potential might be key in producing the high internal concentrations that are sometimes required for function.

510 ## MATERIALS and METHODS

511 ### Protein expression and purification

512 YiiP was expressed in *E. coli* (BL21(DE3)-CodonPlus-RIPL) from a pET vector that
513 included an N-terminal decahistidine tag. Cells were grown in LB media supplemented with 30
514 µg/ml kanamycin at 37°C until they reached an $OD_{600}$ of 0.8. After cooling the media to 20°C,
515 expression was induced by addition of 0.5 mM isopropyl-β-D-thiogalactoside followed by
516 overnight incubation at 20°C. Cells were harvested by centrifugation at 4,000xg for 1 h,
517 resuspended in lysis buffer (20mM HEPES, pH 7.5, 100mM NaCl, 10% glycerol, and 500 µM
518 tris(2-carboxyethyl)phosphine) - 100 ml of buffer per 20 g of cells - and then lysed with a high-
519 pressure homogenizer (Emulsiflex-C3; Avestin, Inc. Ottawa Canada). Protein was extracted
520 from the membrane by adding 1.5 g dodecyl-β-D-maltoside per 100 ml of cell lysate followed by
521 2h of incubation at 4°C. Insoluble material was removed by centrifugation at 100,000xg for 30
522 min. The supernatant was loaded onto a Ni-NTA affinity column pre-equilibrated in buffer A (20
523 mM HEPES, pH 7.5, 100 mM NaCl, 10% glycerol, and 0.05% dodecyl-β-D-maltoside). The
524 column was washed by addition of buffer A supplemented with 20 mM imidazole and protein
525 was then eluted using a gradient of imidazole ranging from 20 to 500 mM. Peak fractions were
526 combined, supplemented with tobacco etch virus (TEV) protease (1:10 weight ratio of TEV:YiiP)
527 to cleave the decahistidine tag, and dialyzed overnight at 4°C against buffer A. TEV protease
528 was removed by loading the dialysate onto an Ni-NTA column and collecting the flow-through
529 fractions. After concentration, a final purification was done with a Superdex 200 size-exclusion
530 chromatography (SEC) column (GE Healthcare, Chicago, Illinois) equilibrated with SEC buffer
531 (20 mM HEPES, pH 7.5,150 mM NaCl, 0.2% n-decyl-β-D-maltoside, and 1 mM tris(2-
532 carboxyethyl)phosphine).

533 Fab selection, modification, expression, and purification has been described previously
534 (Lopez-Redondo et al., 2021). Briefly, the construct designated Fab2r was expressed in *E. coli*
535 strain 55244 from a freshly prepared transformation. Cells were cultured for ~24 h at 30°C with
536 constitutive expression behind an innately leaky T4 promoter. Cell pellets were harvested by
537 centrifugation, lysed with a high-pressure homogenizer and Fab was purified with a 5-ml HiTrap
538 Protein G HP column (GE Healthcare). Pooled fractions were dialyzed against sodium
539 carbonate buffer (pH 5.0) overnight at 4°C and further purified with Resource-S cation exchange
540 column (GE Healthcare). Finally, pure Fab protein was pooled and dialyzed against SEC buffer.

541 ### Cryo-EM sample preparation and structural analyses

542 To ensure that YiiP was fully loaded with $Zn^{2+}$, the purified protein was initially incubated
543 with metal ion chelators (0.5 mM EDTA and 0.5 mM N,N,N′,N′-tetrakis(2-pyridinylmethyl)-1,2-
544 ethanediamine [TPEN]) for 24hrs at 4°C to remove ions that co-purified with the protein, as seen
545 in previous work (Lopez-Redondo et al., 2021). The sample was then dialyzed against YiiP SEC
546 buffer containing 0.5 mM EDTA for 10 h to eliminate chelator-metal complexes. Finally, YiiP was
547 loaded with $Zn^{2+}$ by dialysis (10 h with four buffer exchanges) against SEC buffer supplemented
548 with 0.25 mM $ZnSO_4$. YiiP was then incubated with Fab2r at a 1:1 molar ratio for 1 h at 20°C to
549 form the YiiP-Fab2r complex. This complex was purified by SEC using a Superdex 200 column
550 equilibrated with SEC buffer supplemented with 0.25 mM $ZnSO_4$. Peak fractions at 3-5 mg/ml
551 were used immediately for preparation of cryo-EM samples. Specifically, 3–4 µl were added to
552 glow-discharged grids (C-Flat 1.2/1.3-4Cu-50; Protochips, Inc.) that were blotted under 100%
553 humidity at 4°C and plunged into liquid ethane using a Vitrobot (Thermo Fisher Scientific, Inc.
554 Bridgewater NJ).

555 The YiiP-Fab2r complex was imaged with a Titan Krios G3i electron microscope
556 (Thermo Fisher Scientific, Inc) equipped a Bioquantum energy filter and K2 or K3 direct electron
557 detector (Gatan, Inc. Pleasanton CA) with a pixel size of ~1 Å and a total dose of ~50
558 electrons/Å$^2$. Micrographs containing crystalline ice, excessive contamination, or imaging
559 artifacts were removed and the resulting micrographs were imported into cryoSPARC v2.15
560 (Punjani et al., 2017) for analysis. Particles were picked based on templates generated in
561 previous work and an initial set of particles were subjected to two rounds of 2-D classification to
562 remove false positives. The resulting particles were then subjected to successive rounds of ab
563 initio reconstruction with C1 symmetry and a resolution cutoff starting at 12 Å and declining to 8
564 Å; at each step, the best of two output classes was carried forward to the next round. The
565 resulting particles were used for heterogeneous refinement against two or three reference
566 structures derived from the ab initio jobs, still with C1 symmetry. A final selection of particles
567 was then used for non-uniform refinement using both C1 and C2 symmetry. Postprocessing
568 steps included calculation of local resolution and evaluation of 3-D variability (Punjani and Fleet,
569 2020). For the D70A construct, RELION was used to process a class of particles corresponding
570 to a dimer of dimers (Suppl. Fig. 3). After exporting these particles from cryoSPARC, steps of
571 2D classification and ab initio reconstruction were repeated in RELION, followed by 3D
572 refinement of ~117,000 dimer-of-dimer particles with C2 symmetry. A mask encapsulating one
573 dimer was created with Chimera (Pettersen et al., 2004) and symmetry expansion followed by
574 signal subtraction was used to generate a new set with ~234,000 dimeric particles. This
575 expanded particle set was imported back into cryoSPARC and combined with the class of
576 isolated dimer particles. This combined particle set was used for hetero-refinement to segregate
577 dimer complexes with symmetrical and asymmetrical TMD's. These segregated particle sets
578 were then used for final non-uniform refinement.

579 For model building of symmetrical structures from WT, D287A, D51A, we started with
580 the deposited coordinates from wild type (PDB, 7KZZ). This model was docked as a rigid body
581 to the map and adjusted manually in Coot (Emsley et al., 2010) as a starting structure for
582 refinement using PHENIX (Adams et al., 2010). For D70A and D287A/H263A mutants, the CTD
583 and the TMD from either 7KZZ or 7KZX were separately docked to the map. After adjustment
584 and crude rebuilding in Coot, these models were submitted to NAMDINATOR for Molecular
585 Dynamics Flexible Fitting (Kidmose et al., 2019). The resulting models were used as starting
586 points for PHENIX refinement. This refinement consisted of multiple rounds that alternated
587 between real-space refinement and manual adjustment using Coot. Atomic models were then
588 displayed using CHIMERA (Pettersen et al., 2004) and the PyMOL Molecular Graphics System
589 (Schrödinger, LLC, New York NY).

590 For characterization of cavities running from site A to the cytoplasm, we used Caver
591 Analyst 2.0 Beta (Jurcik et al., 2018). The starting point was defined set near D51 in models for
592 WT and D70A_asym and we selected the shortest tunnel that ran to the cytoplasm. Settings
593 used for the calculations were as follows. Approximation: 12, Minimum probe radius: 0.9,
594 Clustering threshold: 3.5, Shell depth: 2.0, Shell radius: 3.0. $Zn^{2+}$ ions were excluded from the
595 calculation.

596 ## MST experiments

597 YiiP mutants were labelled with Alexa fluor 488 fluorescent dye (Invitrogen life
598 Technologies, Carlsbad CA) by adding 2.5 μL of dye from a 16 mM stock solution in DMSO to
599 200 μL of protein at 1-2 mg/ml in SEC buffer supplemented with 10% glycerol at pH 7. The

reactive group of this dye was N-hydroxysuccinimide, which at pH 7 preferentially targets the N-terminus of the polypeptide. Although labeling of lysine residues is also possible, we believe this was minimal due to the low labeling stoichiometries of ~1:1 used for our experiments. $Zn^{2+}$ was removed by adding 0.5 mM EDTA and 0.5 mM TPEN followed by overnight incubation at 4°C. Excess dye and chelated $Zn^{2+}$ were removed using several cycles of dilution with SEC buffer and concentration with a 50 kDa cutoff concentrator (AMICON, Millipore Sigma, Burlington MA). For titration, $Zn^{2+}$ was buffered either by 0.5 mM sodium citrate or 0.2 mM NTA; the total amount of added $ZnSO_4$ was varied to achieve the desired concentration of free $Zn^{2+}$, according to the program MAXCHELATOR (Bers et al., 1994). Protein concentration during the titration varied from 8 to 100 nM. After 1:1 mixing of protein and $Zn^{2+}$ solutions, samples were centrifuged for 5 min at 2000xg, then loaded into standard treated capillaries for measurement with a Monolith NT.115 MST instrument (NanoTemper Technologies, South San Francisco, CA); measurements were taken at 37 °C with LED power ranges from 20-60% and medium MST power. Data from three independent titrations were analyzed with the MO.Affinity Analysis software v2.3 using MST on-time of 15 s. For determination of $K_d$, data was fitted with a curve based on the law of mass action,

$$F(C_{Zn}) = F_u + \frac{(F_b - F_u) * \left( C_{Zn} + C_P + K_d - \sqrt{(C_{Zn} + C_P + K_d)^2 - 4 * C_P * C_{Zn}} \right)}{2 * C_P}$$

where $F(C_{Zn})$ is the fraction bound, $C_{Zn}$ is concentration of free zinc, $C_P$ is the concentration of YiiP protein, $F_b$ and $F_u$ refer to the normalized fluorescence in the bound and unbound state, and $K_d$ is the affinity constant. Alternatively, the data was fit with the Hill equation to assess cooperativity,

$$F(C_{Zn}) = F_u + \frac{(F_b - F_u)}{1 + \left(\frac{EC_{50}}{C_{Zn}}\right)^n}$$

where $EC_{50}$ is the half-maximal effective concentration (akin to $K_d$) and n is the Hill coefficient.

## Overview of MD simulations

Two types of all-atom, explicit solvent MD simulations were conducted to assess the effects of proton and zinc binding on the structure of the YiiP dimer in a lipid bilayer. We used fixed charge equilibrium MD simulations (using a force field with unchanging parameters) to investigate the interactions between $Zn^{2+}$ ions and YiiP. We also carried out replica exchange constant pH MD (CpHMD) simulations to calculate the p$K_a$ values of all titratable residues and assess the microscopic protonation states of the ion binding sites in the absence of $Zn^{2+}$. Unlike CpHMD simulations, fixed charge simulations do not allow for dynamic protonation or deprotonation of residues. Despite this limitation, they are our preferred approach to study protein-zinc ion interactions and conformational changes because they can be run more efficiently than CpHMD and were thus used to quantify the effect of zinc ions on the structure of YiiP (see Table 5 for a summary of these simulations). The zinc ions in the system were simulated with the non-bonded dummy model described in our previous work (Lopez-Redondo et al., 2021); parameter files are available as package 2934 in the Ligandbook repository (Domański et al., 2017) (https://ligandbook.org/package/2934). Briefly, parameters governing this model were refined based on experimental hydration free energy, ion-oxygen distance and coordination number of the water in the first hydration shell, ultimately reproducing these values

642 with errors of 1% and 0.3%, respectively. The model was further validated using simulations of
643 known zinc-binding proteins, in which stability of the protein and the geometry of the binding
644 complexes were well maintained, though coordination distances were slightly longer than
645 experimental values, especially for sulfur atoms from cysteine residues (Lopez-Redondo et al.,
646 2021). Given that YiiP employs aspartate or histidine residues for $Zn^{2+}$ coordination, the model
647 is well-suited for the current work.

648 ## Fixed charge equilibrium MD simulations

649 MD simulations in the *holo* (with $Zn^{2+}$ in A, B, and C sites) and *apo* (no $Zn^{2+}$) state were
650 taken from our previous study (Lopez-Redondo et al., 2021). To investigate the influence of the
651 binding site B, we generated an "*empty site B"* structure by removing the $Zn^{2+}$ ions from site B in
652 both protomers of PDB ID 5VRF, the same starting structure used previously. In order to study
653 the influence of the salt-bridge D72-R210, simulations were also conducted after applying the
654 D72A mutation to the holo structure (PDB ID 5VRF). In these D72A simulations, $Zn^{2+}$ ions were
655 bound in all sites (A, B, C1, C2), i.e., D72A simulations differed from the holo simulations only in
656 the mutation.

657 The membrane-protein systems were modeled by embedding the YiiP dimer into a 4:1
658 palmitoyloleoylphosphatidylethanolamine:palmitoyloleoylphosphatidylglycerol (POPE:POPG)
659 lipid bilayer, which approximates the composition of the plasma membrane from *E. coli* (Raetz,
660 1986), and solvating the system with water as well as sodium and chloride ions corresponding
661 to a concentration of 100 mM using CHARMM-GUI v1.7 (Jo et al., 2008; Jo et al., 2009; Lee et
662 al., 2016). We used GROMACS 2021.1 (Abraham et al., 2015) with the CHARMM36 force field,
663 the CMAP correction for proteins (MacKerell et al., 1998; Mackerell et al., 2004), CHARMM36
664 lipids (Klauda et al., 2010), and the CHARMM TIP3P water model. The *empty site B* system
665 contained 117,512 atoms, the apo system contained 117,394 atoms, and the D72A system
666 contained 117,418 atoms. All systems were constructed in a hexagonal simulation cell with
667 initial dimensions 101 Å × 101 Å × 135 Å. Default protonation states of all ionizable residues
668 were used based on the experimental pH of 7. The neutral HSD tautomer (proton on the $N_\delta$)
669 was selected to model all histidines except H73 and H155, which were modeled with HSE
670 (proton on the $N_\varepsilon$) based on their orientation relative to $Zn^{2+}$ ions in the cryo-EM structure PDB
671 ID 5VRF.

672 The systems were first energy minimized and underwent a 3.75-ns six-stage
673 equilibration procedure with position restraints on protein and lipids, following the CHARMM-
674 GUI protocol (Jo et al., 2008). Three copies of 1-μs production simulations were carried out with
675 *empty site B*, starting from the same initial system conformation but with different initial
676 velocities. All simulations were performed under periodic boundary conditions at constant
677 temperature ($T$ = 303.15 K) and pressure ($P$ = 1 bar). The velocity rescaling thermostat (Bussi
678 et al., 2007) was used to maintain the temperature with a time constant of 1 ps and separate
679 temperature-coupling groups for protein, lipids, and solvent. A semi-isotropic pressure coupling
680 scheme was implemented using the Parrinello-Rahman barostat (Parrinello and Rahman, 1981)
681 with a time constant of 5 ps, a compressibility of $4.6 \times 10^{-5}$ $bar^{-1}$. Long-range electrostatics were
682 calculated with the smooth particle mesh Ewald method (Essmann et al., 1995) under tinfoil
683 boundary conditions with an initial cutoff of 1.2 nm, which was optimized during the simulation,
684 and interactions beyond the cutoff were calculated in reciprocal space with a fast-Fourier
685 transform on a grid with spacing 0.12-nm and fourth-order spline interpolation. The van der
686 Waals interactions were switched smoothly to 0 between 1.0 nm and 1.2 nm, and the

687 interactions were shifted over the whole range and reduced to 0 at the cutoff. The Verlet
688 neighbor list was updated dynamically by GROMACS for optimized performance with a buffer
689 tolerance of 0.005 kJ/mol/ps. Bonds to hydrogen atoms were treated as rigid holonomic
690 constraints with the P-LINCS algorithm (Hess, 2008) with an expansion order of four and two
691 LINCS iterations; alternatively, SETTLE (Miyamoto and Kollman, 1992) was used for water
692 molecules. The classical equations of motion were integrated with the leapfrog algorithm with a
693 time step of 2 fs.

694 ### CpHMD simulations with pH replica exchange

695 In conventional MD simulations, the protonation states of titratable groups in the system
696 are fixed. To investigate the role of protons in the $Zn^{2+}$ transport of YiiP, we performed
697 membrane-enabled hybrid-solvent continuous constant pH MD simulations (Huang et al., 2021).
698 The currently available implementation of the membrane-enabled CpHMD method does not
699 take into account the direct effect of ions on the titration of nearby residues so we only ran
700 CpHMD simulations for the apo system.

701 CpHMD simulations were initialized with the apo model (PDB ID 5VRF with $Zn^{2+}$ ions
702 removed). An initial 250-ns production simulation was run for the CpHMD apo system to fully
703 relax the membrane, using the same GROMACS 2021.1 protocol described above for fixed
704 charge equilibrium simulations.

705 The membrane-enabled hybrid-solvent continuous CpHMD simulations were performed
706 using the CHARMM program version c42a2 (Brooks et al., 2009) with the PHMD module
707 (Khandogin and Brooks, 2005; Lee et al., 2004) and the pH replica-exchange (REPDSTR)
708 module (Wallace and Shen, 2011). The conformations of YiiP were sampled using conventional
709 all-atom simulations with the CHARMM22/CMAP all-atom force field (MacKerell et al., 1998;
710 Mackerell et al., 2004), the CHARMM36 lipid force field (Klauda et al., 2010), and the CHARMM
711 modified TIP3P water model. The titration coordinates were propagated using the membrane
712 GBSW implicit-solvent model (Im et al., 2003) with the GBSW input radii for the protein taken
713 from Chen et al. (Chen et al., 2006). Based on the average distance between the C2 atoms of
714 the lipids in the cytoplasmic- and periplasmic-facing leaflets, the thickness of the implicit bilayer
715 was set to 40 Å with a switching distance of 5 Å for the transition between the low dielectric slab
716 and bulk solvent. The implicit membrane was excluded by two cylinders with a radius of 14 Å
717 placed at the center of mass of each protomer of YiiP. The radius was selected to maximize the
718 coverage of the interior of the protein with minimal overlapping of the implicit membrane.

719 The final snapshot of the equilibrium simulation was used as the initial structure for the
720 CpHMD simulation. Dummy hydrogen atoms were added to the carboxylate groups of acidic
721 residues following the documentation of the PHMD module (Wallace and Shen, 2011) in
722 CHARMM (Brooks et al., 2009) using the HBUILD facility. The system was then equilibrated
723 with energy minimization using 50 steps of steepest descent followed by 50 steps of adopted
724 basis Newton-Raphson algorithms and CpHMD at pH 7 for 1 ns, whereby the harmonic
725 restraints on the protein heavy atoms were reduced from 1 $kcal \cdot mol^{-1} Å^{-1}$ to zero.

726 The production simulation was then performed using hybrid-solvent CpHMD with the pH
727 replica-exchange protocol (Huang et al., 2021; Wallace and Shen, 2011), using 30 replicas with
728 pH ranging from 1.5 to 11.5. The specific pH conditions were 1.5, 1.75, 2, 2.5, 2.75, 3, 3.25, 3.5,
729 3.75, 4, 4.25, 4.5, 4.75, 5, 5.25, 5.5, 6, 6.5, 7, 7.5, 8, 8.5, 8.75, 9, 9.5, 10, 10.25, 10.5, 11, 11.5,

730 chosen to ensure that the exchange rate between the nearby replicas was higher than 0.2. Each
731 replica was simulated under periodic boundary conditions at constant temperature ($T$ = 303.15
732 K), pressure ($P$ = 1 bar), and specified pH. A modified Hoover thermostat method (Hoover,
733 1985) was used to maintain the temperature, while pressure was maintained using the Langevin
734 piston coupling method (Feller et al., 1995) with a piston mass of 2500 amu. Long-range
735 electrostatics were evaluated with the particle mesh Ewald method (Darden et al., 1993) with a
736 real-space cutoff of 1.2 nm, and interactions beyond the cutoff were calculated in reciprocal
737 space with a fast-Fourier transform on a grid with 0.09-nm spacing and sixth-order spline
738 interpolation. The Lennard–Jones forces were switched smoothly to 0 between 1.0 and 1.2 nm,
739 and the potential was shifted over the whole range and reduced to 0 at the cutoff. Bonds to
740 hydrogen atoms were constrained with the SHAKE algorithm to allow a 2 fs time step. To avoid
741 a spike in potential energy due to a lack of solvent relaxation (Wallace and Shen, 2011), a
742 GBSW calculation was executed every 5 MD steps to update the titration coordinates. An
743 attempt to exchange adjacent pH replicas was made every 1000 MD steps (corresponding to 2
744 ps). Each replica simulation lasted 12 ns for a total aggregate sampling time of 360 ns. Many
745 replicas exchanged across a large fraction of available pH space (Supplementary Figure 7),
746 indicating that 12 ns per replica were sufficient for sampling the degrees of freedom near the
747 protonation sites.

748 ## Analysis of fixed charge MD simulations

749 Analysis of the trajectories was carried out with Python scripts based on MDAnalysis
750 (Gowers et al., 2016). RMSDs of $C_\alpha$ atoms of the whole protein, TMD, and CTD were calculated
751 using the qcprot algorithm (Liu et al., 2010) after optimally superimposing the structure on the
752 same $C_\alpha$ atoms of the cryo-EM structure. Similarly, root mean square fluctuation (RMSF) of $C_\alpha$
753 atoms of the whole protein, TMD, and CTD were calculated. To assess the relative motion
754 between the two domains, a CTD-TMD rotation angle was calculated from the rotation matrix
755 which minimized the RMSD of the CTD after superimposing the protein on the TMD domain of
756 the reference structure (PDB ID 5VRF), as in our previous work (Lopez-Redondo et al., 2021).
757 The existence of the salt-bridge Asp72-Arg210 was quantified using the shortest distance
758 between $O_\delta$ atoms of Asp72 and hydrogen atoms on the side chain of Arg210.

759 ## Analysis of CpHMD simulations

760 The titration coordinates were extracted from CpHMD output files as time series $S(t)$
761 (Supplementary Figure 8) with the CpHMD-Analysis scripts
762 (https://github.com/Hendejac/CpHMD-Analysis). The primary purpose of these simulations is to
763 obtain microscopic p$K_a$ values for titratable residues. We first describe the conventional
764 approach to obtain per-residue p$K_a$ values using the heuristic generalized Hill equation and then
765 in the next section demonstrate an alternative inference approach based directly on statistical
766 mechanics.

767 The deprotonation fraction $S$ of a titratable site was calculated from the titration time
768 series (Supplementary Figure 8) as the number of trajectory frames $N$ of the residue in the
769 deprotonated and protonated states as

770 $$S = \frac{N_{\text{deprot}}}{N_{\text{deprot}} + N_{\text{prot}}}$$

where the site is identified as deprotonated when the CpHMD titration coordinate λ is greater than 0.8 and protonated when the titration coordinate is less than 0.2. Individual residue p$K_a$'s were obtained from a fit to the generalized Henderson-Hasselbalch equation (Hill equation) (Henderson et al., 2020; Huang et al., 2016; Huang et al., 2021) for the deprotonated fraction *S* as a function of pH,

$$S(\mathrm{pH}) = \frac{1}{1 + 10^{n(\mathrm{p}K_a - \mathrm{pH})}}$$

where *n* is the Hill coefficient, which represents the slope of the response curve (Supplementary Figure 9). The mean p$K_a$ of a residue was calculated for each pair of equivalent residues in protomer A and protomer B because these residues were sampled independently in the CpHMD simulation. The statistical error was estimated as the absolute difference between the p$K_a$'s of protomer A and B residues and their mean value.

The CpHMD simulations track the protonation of every single titratable residue and thus provide detailed microscopic information on the exact protonation state for each binding site. The distribution of these microscopic states named S0 to S15 for site A (Supplementary Figure 10, inset table) and S0 to S7 for site B (Supplementary Figure 11, inset table) forms the basis for our alternative calculation of microscopic p$K_a$ values. In order to obtain these CpHMD protonation state distributions, we treated titration coordinate data *S*(*t*) from protomer A and B as independent; thus, by concatenating them we effectively doubled our sampling. Using the same criterion for bound/unbound protons and the definition of microstates for site A (Supplementary Figure 10) and site B (Supplementary Figure 11) we generated separate microstate time series for sites A and B. These time series were then histogrammed to derive the distributions of the microscopic protonation states of site A (Supplementary Figure 10a) and B (Supplementary Figure 11a).

### Calculation of microscopic, state-dependent p$K_a$ values with the *Multibind* method

The *Multibind* method generates thermodynamically consistent models for systems of coupled reactions by using a maximum likelihood approach to combine kinetic or thermodynamic measurements from different sources (Kenney and Beckstein, 2023). Given free energy differences between states (either from simulations or experiments), *Multibind* generates a complete set of free energies for all states in the form of a potential graph that obeys path-independence of free energies and detailed balance while being maximally consistent with the input data. From this set of free energies, all macroscopic thermodynamic observables can be calculated. Without such an approach, thermodynamically inconsistent models arise due to random errors in the input measurements. For $Zn^{2+}$ and proton binding, the free energy differences in the potential graph are calculated as functions of the external parameters, namely the free $Zn^{2+}$ concentration [X] and the pH, and with $\mathrm{p}K_\mathrm{a}$ and $Zn^{2+}$ standard state binding free energy values as input. The binding free energy of a reaction $\mathrm{A} + \mathrm{X} \rightleftharpoons \mathrm{A{:}X}$ is calculated as

$$\beta \Delta G_{\mathrm{bind}}\,([\mathrm{X}]) = \ln\left(\frac{K_\mathrm{D}}{[\mathrm{X}]}\right) = \ln\left(\frac{K_\mathrm{D}}{c_0}\right) - \ln\left(\frac{[\mathrm{X}]}{c_0}\right) = \beta \Delta G^0_{\mathrm{bind}} - \ln\left(\frac{[\mathrm{X}]}{c_0}\right)$$

where $\beta = \frac{1}{k_B T}$ ($k_B$ is Boltzmann's constant), $K_\mathrm{D}$ is the dissociation constant, and the binding free energy is written as a sum of $\Delta G^0_{\mathrm{bind}}$, the binding free energy at the standard state concentration $c_0$=1 M, and a term depending on the ligand concentration [X]. For proton binding, the free energy difference is expressed equivalently as

$$\beta \Delta G_{\text{prot}}\,(\text{pH}) = \ln(10)\,(\text{pH} - \text{p}K_{\text{a}}),$$

where $\text{p}K_{\text{a}}$ is the acid dissociation constant.

We used the Python implementation of *Multibind* (https://github.com/Becksteinlab/multibind) to construct thermodynamic models for binding sites A and B, with the assumption that all binding sites across both protomers are independent. Each model describes the transitions between all possible states as either binding of a proton or binding of a $Zn^{2+}$ ion. With four titratable residues, site A has $M$=$2^4$=16 $Zn^{2+}$-free protonation microstates (states S0 to S15 in Supplementary Figure 10, inset table) and 16 $Zn^{2+}$-bound protonation microstates for a model with 32 states in total (Fig. 4h). Site B has three titratable residues and thus $M$=8 for a model with 16 states in total (states S0 to S7 in Supplementary Figure 11, inset table). Because only free energy differences between states are measurable, we can arbitrarily specify one state as a reference with zero free energy. Here we chose the 0-proton unbound state S0 as the reference state with $G_0$=0, but calculated observables are independent of this particular choice. The probability of observing the system in the microstate $i$ is

$$P_i(\text{pH}, [\text{Zn}^{2+}]) = \frac{1}{Z} e^{-\beta G_{\text{i}}}$$

where $G_i$ is the free energy of any state $i$ and $Z$ is the partition function

$$Z(\text{pH}, [\text{Zn}^{2+}]) = \sum_{k=1}^{M} e^{-\beta G_{k,\text{unbound}}} + \sum_{k=1}^{M} e^{-\beta G_{k,\text{Zn}}}$$

which contains the partition functions of the unbound and bound states. We note that the microstate probabilities $P_i$ can also be directly obtained from the CpHMD simulations, which enables us to use *Multibind* as an inverse method to infer microscopic p$K_a$ from CpHMD data (without resorting to the generalized Hill equation fit), as described below.

The fraction of YiiP protomers that have a $Zn^{2+}$ ion bound to the binding site in question, the *bound fraction*, is

$$\langle \text{X} \rangle = Z^{-1} \sum_{k=1}^{M} e^{-\beta G_{k,\text{Zn}}}$$

The bound fraction can be obtained experimentally from MST measurements.

With the ability to calculate microstate probability or bound fraction at specific pH or $Zn^{2+}$ concentration, we devised an inverse approach to *infer* microscopic, state-dependent p$K_a$'s and standard binding free energies ($\Delta G^0_{\text{bind}}$) from either CpHMD data (to avoid using the Hill equation with the deprotonated fractions, which are aggregated over multiple states and may therefore mask coupling between residues) or from experimental MST measurements.

The inverse *Multibind* approach generates successive microscopic models with a Monte Carlo (MC) scheme and compares the calculated observables to the target values. Observables correspond to microstate probability distributions $P_i$(pH) for CpHMD or bound fraction <X> as a function of pH and $Zn^{2+}$ concentration for MST. Once convergence is reached, the microscopic model contains the inferred microscopic state-dependent p$K_a$ values and $Zn^{2+}$ binding free

848 energies. We implemented a simple finite-temperature MC algorithm that minimizes the RMSD
849 between the given and computed macroscopic features. The model was initialized with p$K_a$
850 values from CpHMD (obtained with the Hill equation) or $\Delta G^0_{bind}$ binding free energies calculated
851 from the experimental $K_d$ from the MST analysis. For each MC step, the target observable was
852 calculated for a range of pH values and $Zn^{2+}$ concentrations. For as long as the RMSD between
853 the computed and the target observable remained above a cutoff (see Table 6), a new set of
854 p$K_a$ or $\Delta G^0_{bind}$ was generated by adding a random value drawn from a uniform distribution
855 ranging from –0.2 to 0.2 p$K_a$ units (for p$K_a$) or –0.2 to 0.2 $k_BT$ (for binding free energies) to all
856 microscopic parameters. A new set of changes was accepted with probability (Metropolis
857 criterion)

858 $$P(\mathrm{p}K_\mathrm{a}, \Delta G^0_\mathrm{bind} \rightarrow \mathrm{p}K_\mathrm{a}', \Delta G^0_\mathrm{bind}{}') = \min(1, e^{-\frac{\Delta \mathrm{RMSD}}{r}})$$

859 where *ΔRMSD* is the difference between the RMSDs between the target and the computed
860 observable for the old set of p$K_a$'s or $\Delta G^0_{bind}$'s and the new set

861 $$\Delta RMSD = RMSD\left(\mathrm{p}K_\mathrm{a}', \Delta G^0_\mathrm{bind}{}'\right) - RMSD(\mathrm{p}K_\mathrm{a}, \Delta G^0_\mathrm{bind})$$

862 The fictional temperature in the Metropolis criterion, *r*, was set to 0.0001 to be on the
863 order of typical per-step changes. The RMSD cutoffs (Table 6) were chosen from initial runs
864 using a zero-temperature MC algorithm, which accepted a new set of changes only when
865 *ΔRMSD* < 0. These initial runs were stopped after 2000 steps and after no changes had been
866 accepted in the last 100 or more steps. The zero-temperature MC ensured that the final set
867 generated the smallest RMSD, while the finite-temperature MC used in the production runs
868 allowed larger parameter space to be sampled. Fifty runs were performed for each target.
869 Averaged p$K_a$ values and corresponding standard deviations were calculated from the 50
870 independent MC runs. Although these standard variations of our parameter estimates weakly
871 depend on the somewhat arbitrary choice of *r*, we chose to report them instead of a rigorous
872 statistical error (which is unavailable with the current approach) to provide a sense of variability
873 of the estimates.

874 For site B, the CpHMD simulations suggested that H73 and H77 behaved identically and
875 had almost the same microscopic p$K_a$ values. We calculated the "coupling energy" (Ullmann,
876 2003) between H73 and H77,

877 $$W = \mathrm{p}K_\mathrm{a}(\mathrm{S0}\rightarrow\mathrm{S2}) - \mathrm{p}K_\mathrm{a}(\mathrm{S1}\rightarrow\mathrm{S3}) = \mathrm{p}K_\mathrm{a}(\mathrm{S0}\rightarrow\mathrm{S1}) - \mathrm{p}K_\mathrm{a}(\mathrm{S2}\rightarrow\mathrm{S3})$$

878 (expressed in p$K_a$ units, i.e. energy divided by $k_BT$ ln10), from the microscopic CpHMD state
879 p$K_a$'s (see Supplementary Data). The coupling energy measures how the protonation of a
880 specific residue (e.g. H73) depends on the protonation of another residue (here, H77). The
881 coupling energy is the difference in p$K_a$ when H77 remains deprotonated while H73 binds a
882 proton (S0→S2, see Supplementary Figure 11) compared to the situation when H77 is already
883 protonated (S1→S3). The H73-H77 coupling energy for the CpHMD simulation was *W*=+1.0 for
884 D70 deprotonated and *W*=+0.2 for D70 protonated. Because *W*>0, binding of a proton to one of
885 the histidines decreases the p$K_a$ of the other, thus decreasing proton binding via anti-
886 cooperative coupling. Preliminary calculations with the MST data, however, showed that small
887 initial differences in the starting values could lead to large p$K_a$ shifts in H73 and H77, with the
888 directions determined by the initial ordering of p$K_a$ values. Because we had no specific evidence
889 that the two histidines should behave differently, we considered the behavior of the initial

890 unconstrained MST inference calculations to be problematic. This problem indicated that the
891 inverse approach can be sensitive to initial values and that there may not always be sufficient
892 target data to constrain the microscopic model. We therefore treated the two residues as
893 symmetrical, i.e., both should be behaving in the same way, and imposed a constraint in the
894 *Multibind* approach so that both were assigned the same p$K_a$ at each step, thus effectively
895 imposing the coupling observed in the CpHMD simulations. The interaction energies between
896 H73 and H77 for the MST-inference data are $W$=+6.2 (D70 deprotonated) and $W$=–0.70 (D70
897 protonated). The dominant state is the one with D70 deprotonated due to the low p$K_a$ of D70
898 and hence the overall behavior of H73 and H77 remains strongly anti-cooperative in the MST-
899 inference model.

900 For Site A, the initial CpHMD simulations did not indicate any degeneracy in p$K_a$ values
901 such as the one for H73/H77 and so no additional constraints were applied for any of the Site A
902 MST-inference calculations. We also calculated the coupling energy for H155 and D159 in site
903 A from the microscopic p$K_a$ values (see Supplementary Data) for the CpHMD and the MST-
904 inference models for (1) no protons bound to D51 and D47 ($W_{MST}$=–5.05, $W_{CpHMD}$=+1.26), (2)
905 D51 protonated ($W_{MST}$=–7.39, $W_{CpHMD}$=+0.59), (3) D51 protonated ($W_{MST}$=–5.26, $W_{CpHMD}$=+1.02),
906 and (4) both D47 and D51 protonated ($W_{MST}$=–2.39, $W_{CpHMD}$=+1.79).Thus, refinement against
907 the experimental MST data changes the model based on the CpHMD results from anti-
908 cooperative binding ($W$>0) to strong cooperative binding ($W$<0).

909 The *inverse* Multibind approach has some limitations when applied to binding curves
910 such as the MST data. The binding isotherms, even when covering a range of pH values, do not
911 contain enough data to determine the microscopic model fully. Therefore, it was necessary to
912 use the CpHMD p$K_a$ values to initialize the model instead of arbitrary starting values. Thus, in
913 the current implementation, the MST inference approach should be viewed as a refinement
914 process for the simulation-derived parameters, restricted or guided by the experimental data.
915 The resulting thermodynamic model allows the calculation of state probabilities (and any other
916 properties) at pH values outside the experimental range but it should be noted that these
917 calculated quantities are extrapolations that may not be accurate due to the lack of experimental
918 data to constrain the model; for instance, conformational changes may occur that could
919 drastically alter the interactions but these changes would not have been captured in a pure
920 binding model such as the one in Fig. 4h.

921 An effective p$K_a$ under the $Zn^{2+}$-free condition was estimated for each residue by fitting
922 the deprotonation fractions (generated from the microscopic *Multibind* model) to the Hill-
923 Langmuir equation. The deprotonation fraction of a specific residue was calculated by summing
924 up the probabilities of microscopic states where the residue was deprotonated. The $Zn^{2+}$
925 concentration was set to $10^{-20}$ M to approximate the $Zn^{2+}$-free condition. For the symmetrized
926 residues H73 and H77, the Hill-Langmuir equation did not produce a satisfactory fit. In order to
927 compute macroscopic p$K_a$'s for such a coupled system, we followed previous work (Henderson
928 et al., 2020; Ullmann, 2003) and fitted the total number of protons bound to the two residues to
929 the so-called "coupled titration model"

930 $$N_{prot} = 2 - [S_1(\mathrm{pH}) + S_2(\mathrm{pH})] = \frac{10^{(\mathrm{p}K_2-\mathrm{pH})} + 2\times 10^{(\mathrm{p}K_1+\mathrm{p}K_2-2\mathrm{pH})}}{1 + 10^{(\mathrm{p}K_1-\mathrm{pH})} + 10^{(\mathrm{p}K_1+\mathrm{p}K_2-2\mathrm{pH})}}$$

931 where $N_{prot}$ is the total number of protons, $S_1$ and $S_2$ are the deprotonation fractions of the two
932 residues, and p$K_1$ and p$K_2$ are the two coupled p$K_a$'s describing the binding of the first proton

933 and the second proton to the coupled titrating sites. These two p$K_a$'s can be interpreted as
934 effective p$K_a$ values of two uncoupled residues.

935

936

## Acknowledgements

We are grateful for help with initial MST experiments from Brian Kloss and Renato Bruni in the Center on Membrane Protein Production and Analysis at the New York Structural Biology Center, which receives funding from NIH grant P41GM116799. Electron microscopy was performed at the Cryo-EM core facility at NYU Langone Health. The authors acknowledge High Performance Computing core facility at NYU Langone Health as well as Research Computing at Arizona State University for providing computational and storage resources that have contributed to the research results reported within this paper. We also thank Bjørn Panella Pederson for critical reading of the manuscript.

Funding for this work was provided by NIH grants R01GM125081 (D.L. Stokes) and R35GM144109 (D.L. Stokes). A portion of this research was also supported by NIH grant U24GM129547 and performed at the PNCC at OHSU and accessed through EMSL (grid.436923.9), a DOE Office of Science User Facility sponsored by the Office of Biological and Environmental Research. MD simulations were performed using PSC Bridges at the Pittsburgh Supercomputing Center (allocation TG-MCB130177), a resource of the Extreme Science and Engineering Discovery Environment, which is supported by National Science Foundation grant ACI-1548562.

## Competing Interests

None.

957 ## References

958


959 Abraham, M.J., Murtola, T., Schulz, R., Páll, S., Smith, J.C., Hess, B., and Lindahl, E. (2015).
960 GROMACS: High performance molecular simulations through multi-level parallelism from
961 laptops to supercomputers. SoftwareX *1--2*, 19 - 25, 10.1016/j.softx.2015.06.001.
962 Adams, P.D., Afonine, P.V., Bunkoczi, G., Chen, V.B., Davis, I.W., Echols, N., Headd, J.J.,
963 Hung, L.W., Kapral, G.J., Grosse-Kunstleve, R.W.*, et al.* (2010). PHENIX: a comprehensive
964 Python-based system for macromolecular structure solution. Acta Crystallogr D Biol
965 Crystallogr *66*, 213-221, 10.1107/S0907444909052925.
966 Alejandro, S., Holler, S., Meier, B., and Peiter, E. (2020). Manganese in Plants: From
967 Acquisition to Subcellular Allocation. Front Plant Sci *11*, 300, 10.3389/fpls.2020.00300.
968 Bers, D.M., Patton, C.W., and Nuccitelli, R. (1994). A practical guide to the preparation of Ca2+
969 buffers. Methods Cell Biol *40*, 3-29, 10.1016/s0091-679x(08)61108-5.
970 Brooks, B.R., Brooks III, C.L., Mackerell Jr., A.D., Nilsson, L., Petrella, R.J., Roux, B., Won, Y.,
971 Archontis, G., Bartels, C., Boresch, S.*, et al.* (2009). CHARMM: The biomolecular simulation
972 program. *30*, 1545-1614, https://doi.org/10.1002/jcc.21287.
973 Bussi, G., Donadio, D., and Parrinello, M. (2007). Canonical sampling through velocity
974 rescaling. Journal of Chemical Physics *126*, 10.1063/1.2408420.
975 Chandrangsu, P., Huang, X., Gaballa, A., and Helmann, J.D. (2019). Bacillus subtilis FolE is
976 sustained by the ZagA zinc metallochaperone and the alarmone ZTP under conditions of
977 zinc deficiency. Mol Microbiol *112*, 751-765, 10.1111/mmi.14314.
978 Chang, Y., Bruni, R., Kloss, B., Assur, Z., Kloppmann, E., Rost, B., Hendrickson, W.A., and Liu,
979 Q. (2014). Structural basis for a pH-sensitive calcium leak across membranes. Science *344*,
980 1131-1135, 10.1126/science.1252043.
981 Chao, Y., and Fu, D. (2004a). Kinetic study of the antiport mechanism of an Escherichia coli
982 zinc transporter, ZitB. J Biol Chem *279*, 12043-12050, 10.1074/jbc.M313510200.
983 Chao, Y., and Fu, D. (2004b). Thermodynamic studies of the mechanism of metal binding to the
984 Escherichia coli zinc transporter YiiP. J Biol Chem *279*, 17173-17180,
985 10.1074/jbc.M400208200.
986 Chen, J.H., Im, W.P., and Brooks, C.L. (2006). Balancing solvation and intramolecular
987 interactions: Toward a consistent generalized born force field. Journal of the American
988 Chemical Society *128*, 3728-3736, 10.1021/ja057216r.
989 Cherezov, V., Hofer, N., Szebenyi, D.M., Kolaj, O., Wall, J.G., Gillilan, R., Srinivasan, V.,
990 Jaroniec, C.P., and Caffrey, M. (2008). Insights into the mode of action of a putative zinc
991 transporter CzrB in Thermus thermophilus. Structure *16*, 1378-1388,
992 10.1016/j.str.2008.05.014.
993 Choi, D.W., and Koh, J.Y. (1998). Zinc and brain injury. Annu Rev Neurosci *21*, 347-375,
994 10.1146/annurev.neuro.21.1.347.
995 Chu, D.S. (2018). Zinc: A small molecule with a big impact on sperm function. PLoS Biol *16*,
996 e2006204, 10.1371/journal.pbio.2006204.
997 Cotrim, C.A., Jarrott, R.J., Martin, J.L., and Drew, D. (2019). A structural overview of the zinc
998 transporters in the cation diffusion facilitator family. Acta Crystallogr D Struct Biol *75*, 357-
999 367, 10.1107/S2059798319003814.
1000 Cotrim, C.A., Jarrott, R.J., Whitten, A.E., Choudhury, H.G., Drew, D., and Martin, J.L. (2021).
1001 Heterologous Expression and Biochemical Characterization of the Human Zinc Transporter
1002 1 (ZnT1) and Its Soluble C-Terminal Domain. Front Chem *9*, 667803,
1003 10.3389/fchem.2021.667803.

1004 Coudray, N., Valvo, S., Hu, M., Lasala, R., Kim, C., Vink, M., Zhou, M., Provasi, D., Filizola, M.,
1005 Tao, J., *et al.* (2013). Inward-facing conformation of the zinc transporter YiiP revealed by
1006 cryoelectron microscopy. Proc Nat Acad Sci *110*, 2140-2145, 10.1073/pnas.1215455110.
1007 Daniels, M.J., Jagielnicki, M., and Yeager, M. (2020). Structure/Function Analysis of human
1008 ZnT8 (SLC30A8): A Diabetes Risk Factor and Zinc Transporter. Curr Res Struct Biol *2*, 144-
1009 155, 10.1016/j.crstbi.2020.06.001.
1010 Darden, T., York, D., and Pedersen, L. (1993). Particle Mesh Ewald - an N.Log(N) Method for
1011 Ewald Sums in Large Systems. Journal of Chemical Physics *98*, 10089-10092, Doi
1012 10.1063/1.464397.
1013 Domański, J., Beckstein, O., and Iorga, B.I. (2017). Ligandbook: an online repository for small
1014 and drug-like molecule force field parameters. Bioinformatics *33*, 1747-1749,
1015 10.1093/bioinformatics/btx037.
1016 Emsley, P., Lohkamp, B., Scott, W., and Cowtan, K. (2010). Features and development of Coot.
1017 Acta Crystallographica Section D - Biological Crystallography *66*, 486-501.
1018 Essmann, U., Perera, L., Berkowitz, M.L., Darden, T., Lee, H., and Pedersen, L.G. (1995). A
1019 Smooth Particle Mesh Ewald Method. Journal of Chemical Physics *103*, 8577-8593, Doi
1020 10.1063/1.470117.
1021 Felle, H., Porter, J.S., Slayman, C.L., and Kaback, H.R. (1980). Quantitative measurements of
1022 membrane potential in Escherichia coli. Biochem *19*, 3585-3590, 10.1021/bi00556a026.
1023 Feller, S.E., Zhang, Y.H., Pastor, R.W., and Brooks, B.R. (1995). Constant-Pressure Molecular-
1024 Dynamics Simulation - the Langevin Piston Method. Journal of Chemical Physics *103*, 4613-
1025 4621, Doi 10.1063/1.470648.
1026 Gayen, A., Leninger, M., and Traaseth, N.J. (2016). Protonation of a glutamate residue
1027 modulates the dynamics of the drug transporter EmrE. Nat Chem Biol *12*, 141-145,
1028 10.1038/nchembio.1999.
1029 Golan, Y., Alhadeff, R., Glaser, F., Ganoth, A., Warshel, A., and Assaraf, Y.G. (2018).
1030 Demonstrating aspects of multiscale modeling by studying the permeation pathway of the
1031 human ZnT2 zinc transporter. PLoS Comput Biol *14*, e1006503,
1032 10.1371/journal.pcbi.1006503.
1033 Golan, Y., Alhadeff, R., Warshel, A., and Assaraf, Y.G. (2019). ZnT2 is an electroneutral proton-
1034 coupled vesicular antiporter displaying an apparent stoichiometry of two protons per zinc
1035 ion. PLoS Comput Biol *15*, e1006882, 10.1371/journal.pcbi.1006882.
1036 Gottesman, N., Asraf, H., Bogdanovic, M., Sekler, I., Tzounopoulos, T., Aizenman, E., and
1037 Hershfinkel, M. (2022). ZnT1 is a neuronal Zn(2+)/Ca(2+) exchanger. Cell Calcium *101*,
1038 102505, 10.1016/j.ceca.2021.102505.
1039 Gowers, R.J., Linke, M., Barnoud, J., Reddy, T.J.E., Melo, M.N., Seyler, S.L., Dotson, D.L.,
1040 Domański, J., Buchoux, S., Kenney, I.M., *et al.* (2016). MDAnalysis: A Python package for
1041 the rapid analysis of molecular dynamics simulations. Paper presented at: Proceedings of
1042 the 15th Python in Science Conference (Austin, TX: SciPy).
1043 Guffanti, A.A., Wei, Y., Rood, S.V., and Krulwich, T.A. (2002). An antiport mechanism for a
1044 member of the cation diffusion facilitator family: divalent cations efflux in exchange for K+
1045 and H+. Mol Microbiol *45*, 145-153.
1046 Gupta, S., Chai, J., Cheng, J., D'Mello, R., Chance, M.R., and Fu, D. (2014). Visualizing the
1047 kinetic power stroke that drives proton-coupled zinc(II) transport. Nature *512*, 101-104,
1048 10.1038/nature13382.
1049 Han, B.B., Watanabe, S., Nomura, N., Liu, K., Uemura, T., Inoue, M., Tsutsumi, A., Fujita, H.,
1050 Kinoshita, K., Iwata, S., *et al.* (2022). Cryo-EM structures of human zinc transporter ZnT7
1051 reveal the mechanism of Zn<sup>2+</sup> uptake into the Golgi apparatus. bioRxiv.
1052 Hara, T., Takeda, T.A., Takagishi, T., Fukue, K., Kambe, T., and Fukada, T. (2017).
1053 Physiological roles of zinc transporters: molecular and genetic importance in zinc
1054 homeostasis. J Physiol Sci *67*, 283-301, 10.1007/s12576-017-0521-4.

Henderson, J.A., Huang, Y., Beckstein, O., and Shen, J. (2020). Alternative proton-binding site and long-distance coupling in Escherichia coli sodium-proton antiporter NhaA. Proc Natl Acad Sci U S A *117*, 25517-25522, 10.1073/pnas.2005467117.

Hess, B. (2008). P-LINCS: A Parallel Linear Constraint Solver for Molecular Simulation. J Chem Theory Comput *4*, 116-122, 10.1021/ct700200b.

Hoch, E., Lin, W., Chai, J., Hershfinkel, M., Fu, D., and Sekler, I. (2012). Histidine pairing at the metal transport site of mammalian ZnT transporters controls Zn2+ over Cd2+ selectivity. Proc Nat Acad Sci *109*, 7202-7207, 10.1073/pnas.1200362109.

Hoover, W.G. (1985). Canonical Dynamics - Equilibrium Phase-Space Distributions. Physical Review A *31*, 1695-1697, DOI 10.1103/PhysRevA.31.1695.

Huang, Y., Chen, W., Dotson, D.L., Beckstein, O., and Shen, J. (2016). Mechanism of pH-dependent activation of the sodium-proton antiporter NhaA. Nat Commun *7*, 12940, 10.1038/ncomms12940.

Huang, Y., Henderson, J.A., and Shen, J. (2021). Continuous Constant pH Molecular Dynamics Simulations of Transmembrane Proteins. In Structure and Function of Membrane Proteins, I. Schmidt-Krey, and J.C. Gumbart, eds. (New York, NY: Springer US), pp. 275-287.

Im, W.P., Lee, M.S., and Brooks, C.L. (2003). Generalized born model with a simple smoothing function. Journal of Computational Chemistry *24*, 1691-1702, 10.1002/jcc.10321.

Isom, D.G., Castaneda, C.A., Cannon, B.R., Velu, P.D., and Garcia-Moreno, E.B. (2010). Charges in the hydrophobic interior of proteins. Proc Natl Acad Sci U S A *107*, 16096-16100, 10.1073/pnas.1004213107.

Jarmoskaite, I., AlSadhan, I., Vaidyanathan, P.P., and Herschlag, D. (2020). How to measure and evaluate binding affinities. Elife *9*, ARTN e57264 10.7554/eLife.57264.

Jo, S., Kim, T., Iyer, V.G., and Im, W. (2008). CHARMM-GUI: a web-based graphical user interface for CHARMM. J Comput Chem *29*, 1859-1865, 10.1002/jcc.20945.

Jo, S., Lim, J.B., Klauda, J.B., and Im, W. (2009). CHARMM-GUI Membrane Builder for Mixed Bilayers and its Application to Yeast Membranes. Biophys J *97*, 50--58, 10.1016/j.bpj.2009.04.013.

Jurcik, A., Bednar, D., Byska, J., Marques, S.M., Furmanova, K., Daniel, L., Kokkonen, P., Brezovsky, J., Strnad, O., Stourac, J.*, et al.* (2018). CAVER Analyst 2.0: analysis and visualization of channels and tunnels in protein structures and molecular dynamics trajectories. Bioinformatics *34*, 3586-3588, 10.1093/bioinformatics/bty386.

Kambe, T., Tsuji, T., Hashimoto, A., and Itsumura, N. (2015). The Physiological, Biochemical, and Molecular Roles of Zinc Transporters in Zinc Homeostasis and Metabolism. Physiol Rev *95*, 749-784, 10.1152/physrev.00035.2014.

Kenney, I., and Beckstein, O. (2023). Thermodynamically consistent determination of free energies and rates in kinetic cycle models. 2023.2004.2008.536126, 10.1101/2023.04.08.536126.

Khandogin, J., and Brooks, C.L. (2005). Constant pH molecular dynamics with proton tautomerism. Biophys J *89*, 141-157, 10.1529/biophysj.105.061341.

Kidmose, R.T., Juhl, J., Nissen, P., Boesen, T., Karlsen, J.L., and Pedersen, B.P. (2019). Namdinator - automatic molecular dynamics flexible fitting of structural models into cryo-EM and crystallography experimental maps. IUCrJ *6*, 526-531, 10.1107/S2052252519007619.

Klauda, J.B., Venable, R.M., Freites, J.A., O'Connor, J.W., Tobias, D.J., Mondragon-Ramirez, C., Vorobyov, I., MacKerell, J., Alexander D, and Pastor, R.W. (2010). Update of the CHARMM all-atom additive force field for lipids: validation on six lipid types. J Phys Chem B *114*, 7830-7843, 10.1021/jp101759q.

Lee, J., Cheng, X., Swails, J.M., Yeom, M.S., Eastman, P.K., Lemkul, J.A., Wei, S., Buckner, J., Jeong, J.C., Qi, Y.*, et al.* (2016). CHARMM-GUI Input Generator for NAMD, GROMACS,

1104 AMBER, OpenMM, and CHARMM/OpenMM Simulations Using the CHARMM36 Additive
1105 Force Field. J Chem Theory Comput *12*, 405-413, 10.1021/acs.jctc.5b00935.
1106 Lee, M.S., Salsbury, F.R., Jr., and Brooks, C.L., 3rd (2004). Constant-pH molecular dynamics
1107 using continuous titration coordinates. Proteins *56*, 738-752, 10.1002/prot.20128.
1108 Liang, X., Dempski, R.E., and Burdette, S.C. (2016). Zn(2+) at a cellular crossroads. Curr Opin
1109 Chem Biol *31*, 120-125, 10.1016/j.cbpa.2016.02.008.
1110 Liu, P., Agrafiotis, D.K., and Theobald, D.L. (2010). Fast determination of the optimal rotational
1111 matrix for macromolecular superpositions. J Comput Chem *31*, 1561-1563,
1112 10.1002/jcc.21439.
1113 Lonergan, Z.R., and Skaar, E.P. (2019). Nutrient Zinc at the Host-Pathogen Interface. Trends
1114 Biochem Sci *44*, 1041-1056, 10.1016/j.tibs.2019.06.010.
1115 Lopez-Redondo, M., Fan, S., Koide, A., Koide, S., Beckstein, O., and Stokes, D.L. (2021). Zinc
1116 binding alters the conformational dynamics and drives the transport cycle of the cation
1117 diffusion facilitator YiiP. J Gen Physiol *153*, 10.1085/jgp.202112873.
1118 Lopez-Redondo, M.L., Coudray, N., Zhang, Z., Alexopoulos, J., and Stokes, D.L. (2018).
1119 Structural basis for the alternating access mechanism of the cation diffusion facilitator YiiP.
1120 Proc Natl Acad Sci U S A, 10.1073/pnas.1715051115.
1121 Lu, M., Chai, J., and Fu, D. (2009). Structural basis for autoregulation of the zinc transporter
1122 YiiP. Nature structural & molecular biology *16*, 1063-1067, 10.1038/nsmb.1662.
1123 Lu, M., and Fu, D. (2007). Structure of the zinc transporter YiiP. Science *317*, 1746-1748,
1124 10.1126/science.1143748.
1125 MacKerell, A.D., Bashford, D., Bellott, M., Dunbrack, R.L., Evanseck, J.D., Field, M.J., Fischer,
1126 S., Gao, J., Guo, H., Ha, S.*, et al.* (1998). All-atom empirical potential for molecular modeling
1127 and dynamics studies of proteins. J Phys Chem B *102*, 3586-3616, 10.1021/jp973084f.
1128 Mackerell, A.D., Jr., Feig, M., and Brooks, C.L., 3rd (2004). Extending the treatment of
1129 backbone energetics in protein force fields: limitations of gas-phase quantum mechanics in
1130 reproducing protein conformational distributions in molecular dynamics simulations. J
1131 Comput Chem *25*, 1400-1415, 10.1002/jcc.20065.
1132 Maret, W. (2013). Zinc biochemistry: from a single zinc enzyme to a key element of life. Adv
1133 Nutr *4*, 82-91, 10.3945/an.112.003038.
1134 Miyamoto, S., and Kollman, P.A. (1992). Settle - an Analytical Version of the Shake and Rattle
1135 Algorithm for Rigid Water Models. Journal of Computational Chemistry *13*, 952-962, DOI
1136 10.1002/jcc.540130805.
1137 Montanini, B., Blaudez, D., Jeandroz, S., Sanders, D., and Chalot, M. (2007). Phylogenetic and
1138 functional analysis of the Cation Diffusion Facilitator (CDF) family: improved signature and
1139 prediction of substrate specificity. BMC genomics *8*, 107, 10.1186/1471-2164-8-107.
1140 Morrison, E.A., Robinson, A.E., Liu, Y., and Henzler-Wildman, K.A. (2015). Asymmetric
1141 protonation of EmrE. J Gen Physiol *146*, 445-461, 10.1085/jgp.201511404.
1142 Outten, C.E., and O'Halloran, T.V. (2001). Femtomolar sensitivity of metalloregulatory proteins
1143 controlling zinc homeostasis. Science *292*, 2488-2492, 10.1126/science.1060331.
1144 Panahi, A., and Brooks, C.L., 3rd (2015). Membrane environment modulates the pKa values of
1145 transmembrane helices. J Phys Chem B *119*, 4601-4607, 10.1021/acs.jpcb.5b00289.
1146 Parrinello, M., and Rahman, A. (1981). Polymorphic transitions in single crystals: A new
1147 molecular dynamics method. J~Appl~Phys *52*, 7182-7190, 10.1063/1.328693.
1148 Parsons, D.S., Hogstrand, C., and Maret, W. (2018). The C-terminal cytosolic domain of the
1149 human zinc transporter ZnT8 and its diabetes risk variant. FEBS J *285*, 1237-1250,
1150 10.1111/febs.14402.
1151 Pettersen, E.F., Goddard, T.D., Huang, C.C., Couch, G.S., Greenblatt, D.M., Meng, E.C., and
1152 Ferrin, T.E. (2004). UCSF Chimera--a visualization system for exploratory research and
1153 analysis. J Comput Chem *25*, 1605-1612.

Punjani, A., and Fleet, D.J. (2020). 3D Variability Analysis: Resolving continuous flexibility and discrete heterogeneity from single particle cryo-EM. 2020.2004.2008.032466, 10.1101/2020.04.08.032466 %J bioRxiv.

Punjani, A., Rubinstein, J.L., Fleet, D.J., and Brubaker, M.A. (2017). cryoSPARC: algorithms for rapid unsupervised cryo-EM structure determination. Nat Methods *14*, 290-296, 10.1038/nmeth.4169.

Raetz, C.R. (1986). Molecular genetics of membrane phospholipid synthesis. Annu Rev Genet *20*, 253-295, 10.1146/annurev.ge.20.120186.001345.

Robinson, N.J., and Winge, D.R. (2010). Copper metallochaperones. Annu Rev Biochem *79*, 537-562, 10.1146/annurev-biochem-030409-143539.

Sala, D., Giachetti, A., and Rosato, A. (2019). An atomistic view of the YiiP structural changes upon zinc(II) binding. Biochim Biophys Acta Gen Subj *1863*, 1560-1567, 10.1016/j.bbagen.2019.06.001.

Sharma, G., and Merz, K.M. (2022). Mechanism of Zinc Transport through the Zinc Transporter YiiP. J Chem Theory Comput *18*, 2556-2568, 10.1021/acs.jctc.1c00927.

Shusterman, E., Beharier, O., Shiri, L., Zarivach, R., Etzion, Y., Campbell, C.R., Lee, I.H., Okabayashi, K., Dinudom, A., Cook, D.I.*, et al.* (2014). ZnT-1 extrudes zinc from mammalian cells functioning as a Zn(2+)/H(+) exchanger. Metallomics *6*, 1656-1663, 10.1039/c4mt00108g.

Tanford, C. (1983). Translocation pathway in the catalysis of active transport. Proc Natl Acad Sci (USA) *80*, 3701-3705.

Udagedara, S.R., La Porta, D.M., Spehar, C., Purohit, G., Hein, M.J.A., Fatmous, M.E., Casas Garcia, G.P., Ganio, K., McDevitt, C.A., and Maher, M.J. (2020). Structural and functional characterizations of the C-terminal domains of CzcD proteins. J Inorg Biochem *208*, 111087, 10.1016/j.jinorgbio.2020.111087.

Ullmann, G.M. (2003). Relations between protonation constants and titration curves in polyprotic acids: A critical view. Journal of Physical Chemistry B *107*, 1263-1271, 10.1021/jp026454v.

Wallace, J.A., and Shen, J.K. (2011). Continuous Constant pH Molecular Dynamics in Explicit Solvent with pH-Based Replica Exchange. J Chem Theory Comput *7*, 2617-2629, 10.1021/ct200146j.

Xue, J., Xie, T., Zeng, W., Jiang, Y., and Bai, X.C. (2020). Cryo-EM structures of human ZnT8 in both outward- and inward-facing conformations. Elife *9*, 10.7554/eLife.58823.

Yin, S., Duan, M., Fang, B., Zhao, G., Leng, X., and Zhang, T. (2022). Zinc homeostasis and regulation: Zinc transmembrane transport through transporters. Crit Rev Food Sci Nutr, 1-11, 10.1080/10408398.2022.2048292.

Yue, Z., Chen, W., Zgurskaya, H.I., and Shen, J.N. (2017). Constant pH Molecular Dynamics Reveals How Proton Release Drives the Conformational Transition of a Transmembrane Efflux Pump. Journal of Chemical Theory and Computation *13*, 6405-6414, 10.1021/acs.jctc.7b00874.

Zeytuni, N., Uebe, R., Maes, M., Davidov, G., Baram, M., Raschdorf, O., Nadav-Tsubery, M., Kolusheva, S., Bitton, R., Goobes, G.*, et al.* (2014). Cation diffusion facilitators transport initiation and regulation is mediated by cation induced conformational changes of the cytoplasmic domain. PLoS One *9*, e92141, 10.1371/journal.pone.0092141.

Zhang, S.F., Fu, C.T., Luo, Y.B., Xie, Q.R., Xu, T., Sun, Z.Y., Su, Z.M., and Zhou, X.M. (2023). Cryo-EM structure of a eukaryotic zinc transporter at a low pH suggests its Zn2+-releasing mechanism. J Struct Biol *215*, ARTN 107926 10.1016/j.jsb.2022.107926.

1202

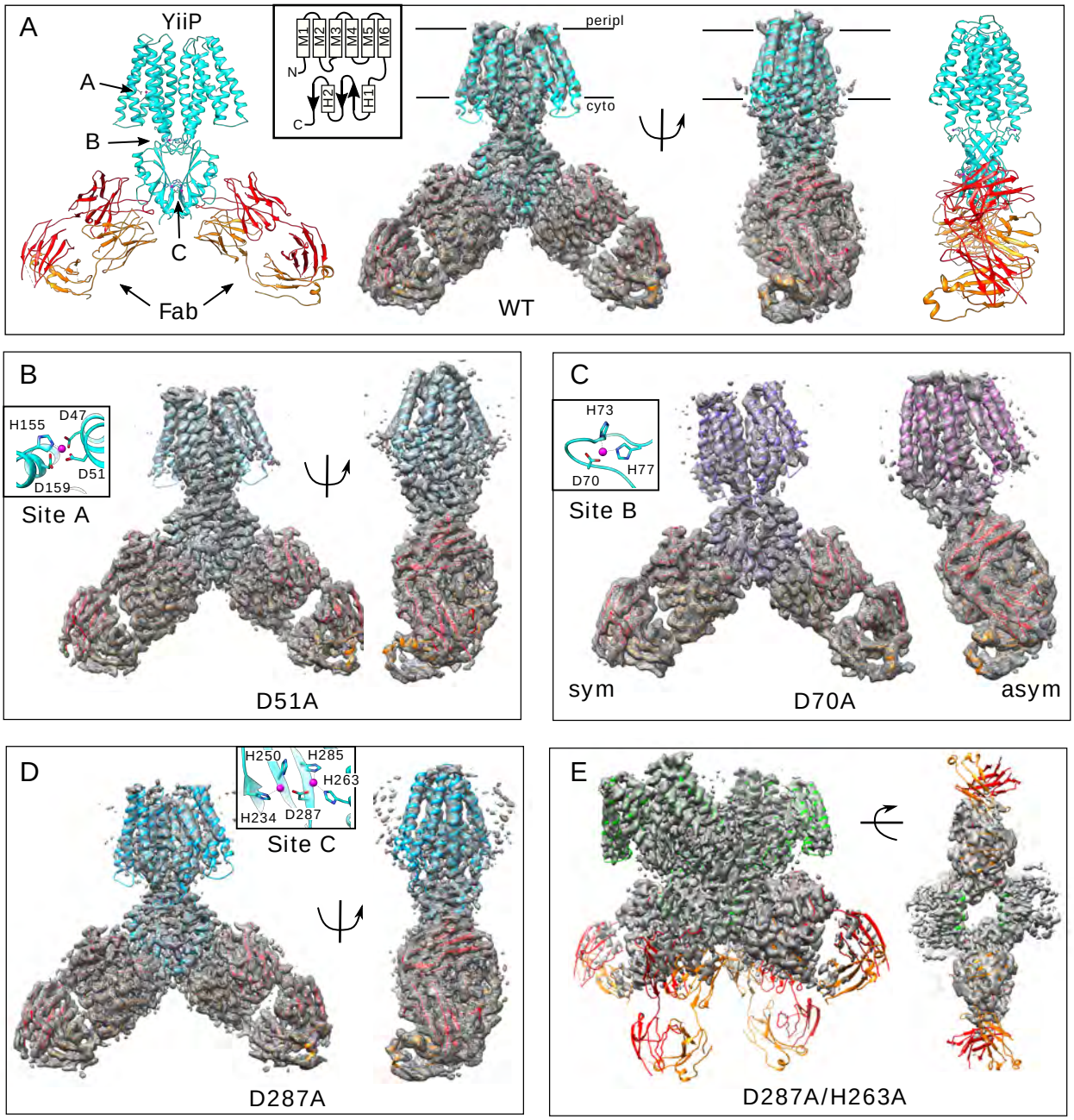
A
YiiP
A
B
C
Fab
M1
M2
M3
M4
M5
M6
H2
H1
N
C
peripl
cyto
WT
B
H155
D47
D51
D159
Site A
D51A
C
H73
H77
D70
Site B
sym
D70A
asym
D
H250
H285
H263
H234
D287
Site C
D287A
E
D287A/H263A

Figure 1

1203

1204 Figure 1. Overview of the cryo-EM structures.

1205 Density maps and corresponding atomic models are shown for each mutant. Fab molecules are
1206 colored orange (light chain) and red (heavy chain) with YiiP colored in cyan, blue, purple and
1207 green, depending on the mutant. The homo-dimers adopt C2 symmetry for WT (A), D51A (B)
1208 and D287A (D) mutants, but a bend between TMD and CTD break this symmetry for D70A (C).
1209 The D287A/H263A mutant (E) forms a dimer of dimers in which the Fab molecules are rather
1210 disordered. Two conformations were observed for D70A, both of which are shown in panel C:
1211 D70A_sym on the left and D70A_asym on the right. Location $Zn^{2+}$ binding sites, membrane
1212 boundaries as well as the topology of the YiiP protomer (inset) are shown in panel A; rectangles
1213 and arrows represent $\alpha$-helices and $\beta$-sheets, respectively. Insets in panels B-D show the
1214 coordination geometry at the individual sites. Although the resolution was not always sufficient
1215 to uniquely define the side chain orientations, the maps are fully consistent with coordination
1216 geometry originally defined in the higher resolution X-ray structure (Lu et al., 2009).

1217

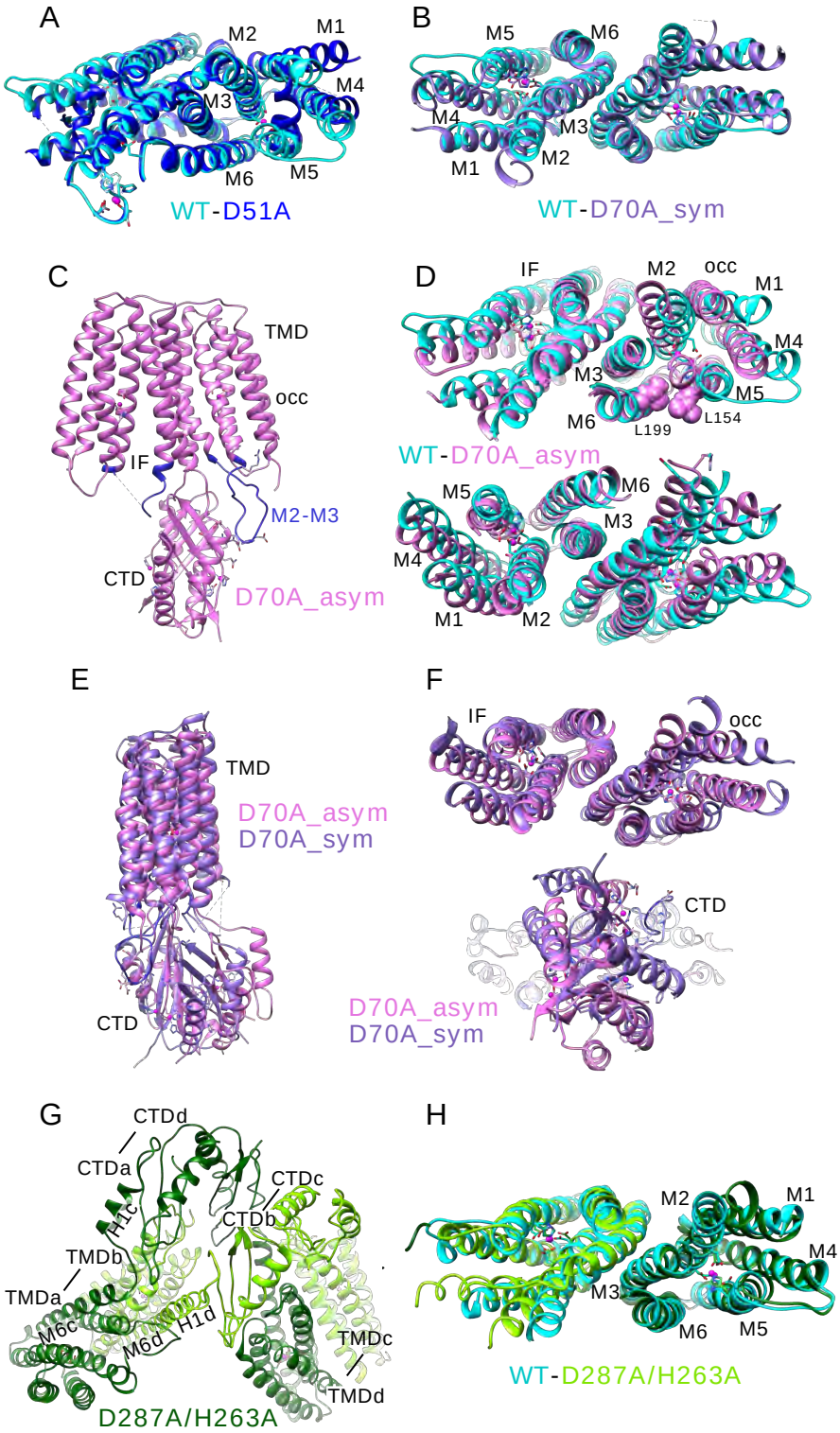
A
M2
M1
M4
M3
M6
M5
WT-D51A
B
M5
M6
M4
M3
M1
M2
WT-D70A_sym
C
TMD
occ
IF
M2-M3
CTD
D70A_asym
D
IF
M2
occ
M1
M4
M3
M5
M6
L199
L154
WT-D70A_asym
M5
M6
M3
M4
M1
M2
E
TMD
D70A_asym
D70A_sym
CTD
F
IF
occ
CTD
D70A_asym
D70A_sym
G
CTDd
CTDa
CTDc
H1c
CTDb
TMDb
TMDa
M6c
M6d
H1d
TMDc
TMDd
D287A/H263A
H
M2
M1
M4
M3
M6
M5
WT-D287A/H263A

Figure 2

1218 Figure 2. Comparisons of atomic models.

1219 (A) Overlay of the TMD for WT (cyan) and D51A (blue) structures. This view is from the
1220 cytoplasmic side of the membrane, tilted slightly to show site A in protomer A. Core helices (M2,
1221 M3, M6) are well aligned, but there are substantial displacements of the peripheral helices (M1,
1222 M4, M5), presumably due to lack of $Zn^{2+}$ binding at site A serving to bridge M2 and M5. (B)
1223 Overlay of the TMD for WT (cyan) and D70A_sym (purple) shows a very similar configuration of
1224 helices and an intact dimeric interface. This view is directly along the two-fold axis from the
1225 cytoplasmic side of the membrane. (C) Structure of D70A_asym viewed along the membrane
1226 plane showing the asymmetry between the two TMD's. The protomer on the left (chain B)
1227 adopts an IF conformation, whereas the protomer on the right (chain A) adopts a novel occluded
1228 conformation that includes a reconfigured TM2/TM3 loop (blue) making a novel interaction with
1229 the CTD. (D) Overlay of the TMD for WT (cyan) and D70A_asym (plum) showing the occluded
1230 conformation adopted by protomer A (top) and the IF conformation adopted by protomer B
1231 (bottom). L199 and L154 (spheres) make van der Waals interactions that appear to stabilize the
1232 occluded conformation. These views are from the cytoplasmic side of the membrane, slightly
1233 tilted to show the respective protomers. (E-F) Overlays of D70A_asym (plum) and D70A_sym
1234 (purple) structures after alignment of core helices TM3 and TM6. Structures are viewed parallel
1235 to the membrane plane in E and along the two-fold axis from the cytoplasmic side of the
1236 membrane in F. A significant shift in the position of the CTD is apparent in E and bottom panel
1237 in F. Despite this shift and substantial conformational changes in the occluded protomer A, the
1238 dimer interface in the TMD (TM3 and TM6) is well aligned (F, top panel). (G) Domain swapped
1239 dimer of dimers adopted by the D287A/H263A construct. Dimerization of TMD's involves
1240 interaction between one dark-green and one light-green molecule (e.g., TMDa and TMDb,
1241 where "a" and "b" refer to chain ID), whereas dimerization of CTD's involves interaction between
1242 either two dark-green or two light-green molecules (e.g., CTDa and CTDd). The linker between
1243 M6 and the CTD adopts a long straight helix in chains b and d, but remains an unstructured loop
1244 in chains a and c. This view is from the cytoplasm looking toward the membrane surface. (H)
1245 Overlay of the TMD for WT (cyan) and D287A/H263A structures viewed along the dimer axis
1246 from the cytoplasmic side of the membrane shows a good match, indicating that disruption of
1247 site C affects mainly the configuration of the CTD.

1248

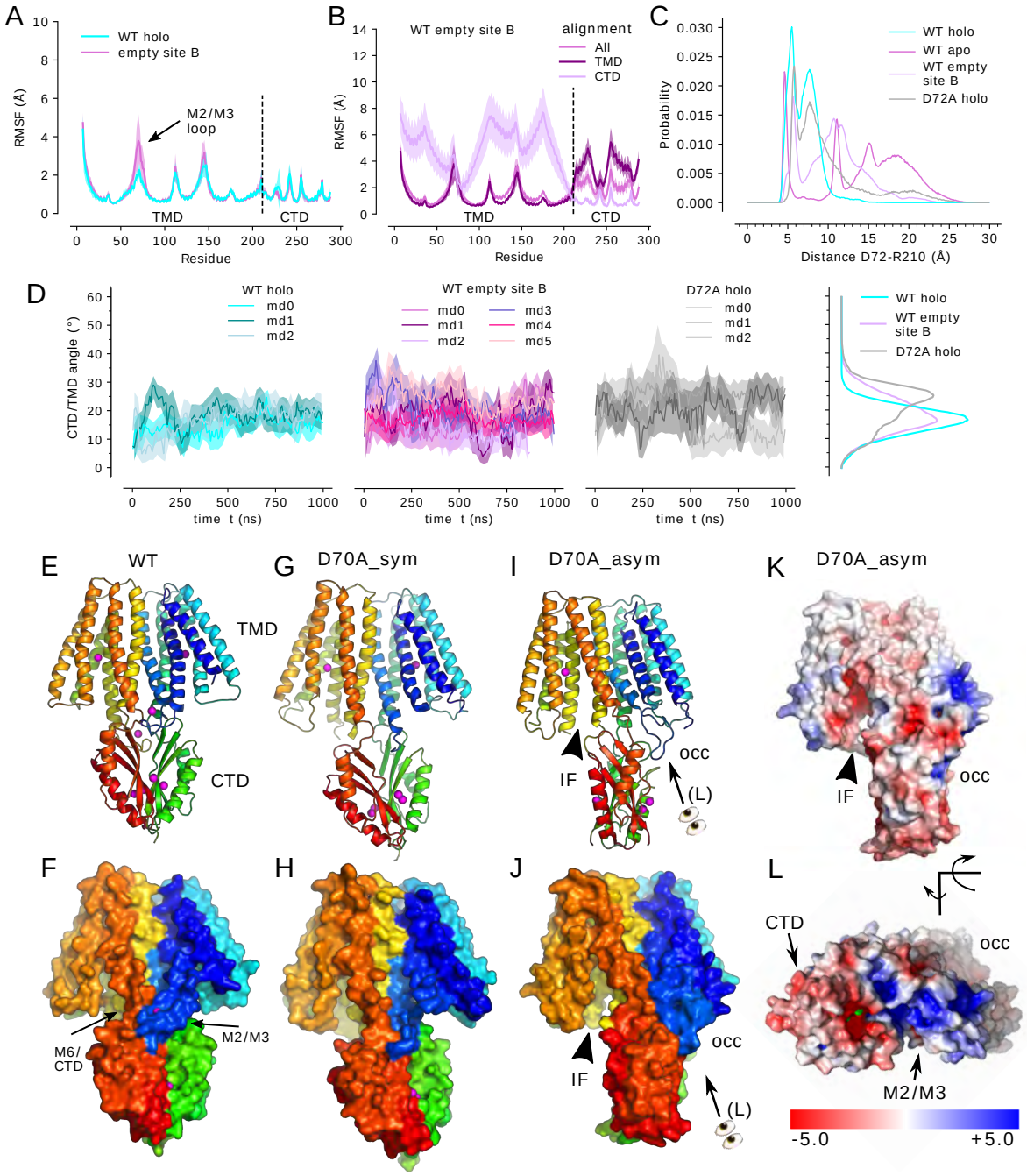
A
WT holo
empty site B
M2/M3
loop
RMSF (Å)
TMD
CTD
Residue
B
WT empty site B
alignment
All
TMD
CTD
RMSF (Å)
Residue
C
WT holo
WT apo
WT empty
site B
D72A holo
Probability
Distance D72-R210 (Å)
D
WT holo
md0
md1
md2
WT empty site B
md0
md1
md2
md3
md4
md5
D72A holo
md0
md1
md2
CTD/TMD angle (°)
time t (ns)
WT holo
WT empty
site B
D72A holo
E
WT
TMD
CTD
G
D70A_sym
I
D70A_asym
IF
occ
(L)
K
D70A_asym
IF
occ
F
M6/
CTD
M2/M3
H
J
IF
occ
(L)
L
CTD
occ
M2/M3
-5.0
+5.0

Figure 3

1249 Figure 3. $Zn^{2+}$ removal from site B in the TM2/TM3 loop.

1250 (A) Per-residue RMSF of the WT, holo structure with $Zn^{2+}$ present (cyan) and absent (purple) at
1251 site B demonstrates a notable increase in fluctuations in the TM2/TM3 loop. The dashed line
1252 indicates the boundary between TMD and CTD. (B) Per-residue RMSF for simulations with
1253 empty site B using three different alignment schemes: the entire molecule ("All"),
1254 transmembrane domain ("TMD"), or C-terminal domain ("CTD"). Analogous data for the WT,
1255 holo structure have previously been published (Fig. 3i in Lopez-Redondo et al., 2021). (C)
1256 Distributions of distance between $C\alpha$ atoms from Asp72 in one chain and Arg210 in the
1257 opposite chain during simulations of the WT, holo structure, WT apo structure with $Zn^{2+}$ absent
1258 from all sites, WT structure with site B empty, and the D72A mutant with $Zn^{2+}$ present at all three
1259 sites. The sharp peak at ~5 Å from the holo structure suggests a salt bridge that is less stable in
1260 the D72A mutant and disrupted when $Zn^{2+}$ is absent from site B. (D) Angle between the TMD
1261 and CTD in simulations in the presence (cyan) and absence (purple) of $Zn^{2+}$ at site B; the D72A
1262 mutant in the holo state is also shown on the right. The distribution of angles, on the right,
1263 highlight greater mobility either with site B is empty or with the D72A mutation. (E,F) Structure of
1264 the WT, holo YiiP dimer showing global C2 symmetry about a vertical axis and juxtaposition of
1265 the TM2/3 loop (blue) with the TM6/CTD linker from the opposing protomer (orange-to-red).
1266 Rainbow colors progress from blue to red moving from the N-terminus of one protomer to the C-
1267 terminus of the other protomer. (G,H) D70A_sym structure shows a kink between TMD and
1268 CTD and disordering of the TM2/3 loop. Both protomers are in the IF state. (I,J) D70A_asym
1269 structure showing further twisting of the CTD and asymmetry of the TMD's. The TM2/3 loop is
1270 disordered in the protomer on the left (chain B), but adopts a novel interaction with the CTD in
1271 the protomer on the right (chain A). (K,L). Electrostatic surface of D70A_asym showing a
1272 negatively charged cavity leading to site A on the left, but an occluded cavity with positive
1273 charge on the right. Note that L is at an oblique angle looking down on the M2-M3 loop.

1274

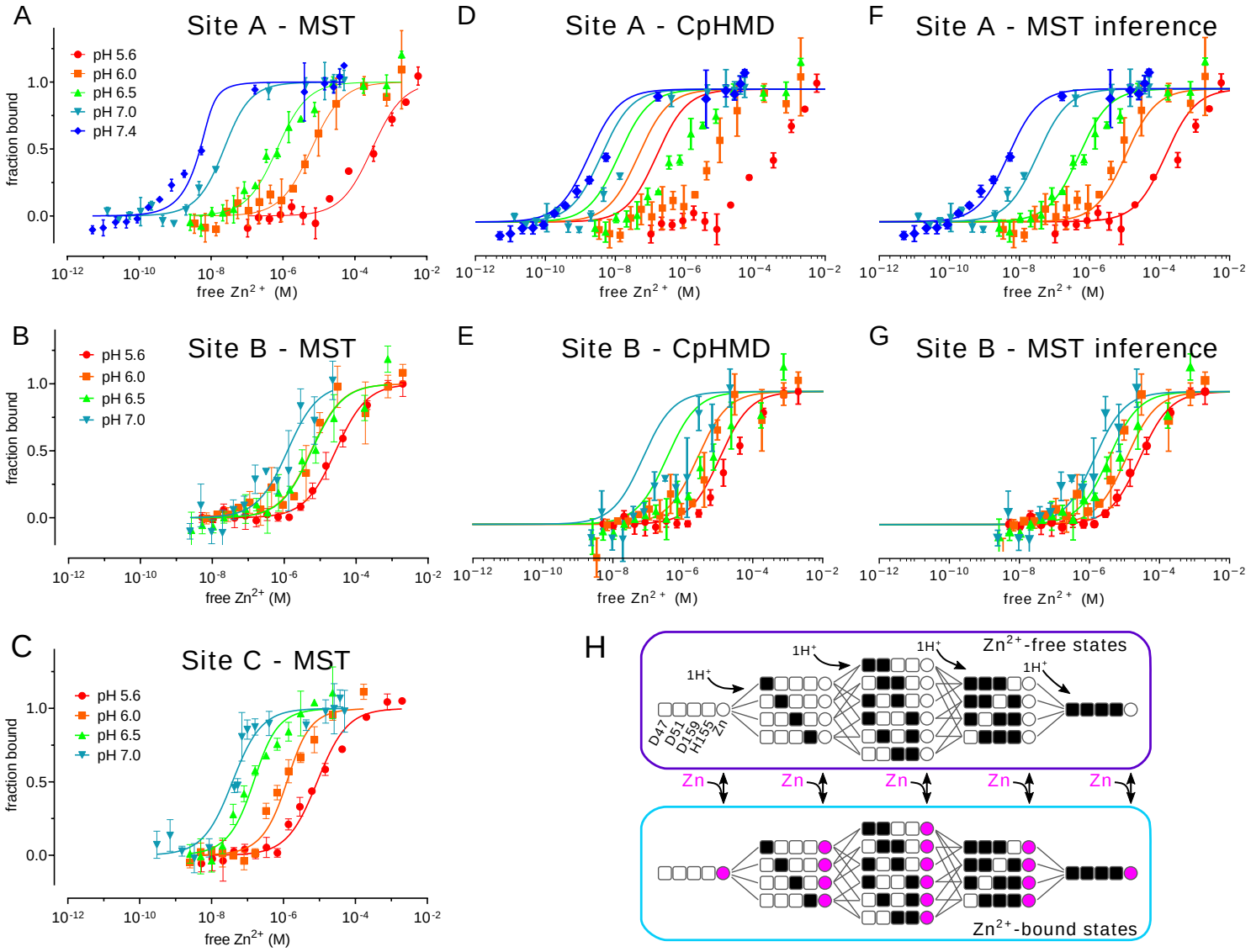
A
Site A - MST
pH 5.6
pH 6.0
pH 6.5
pH 7.0
pH 7.4
fraction bound
free Zn2+ (M)
D
Site A - CpHMD
F
Site A - MST inference
B
Site B - MST
E
Site B - CpHMD
G
Site B - MST inference
C
Site C - MST
H
Zn2+-free states
1H+
D47
D51
D159
H159
Zn
Zn2+-bound states

Figure 4

1275 Figure 4. pH dependence of $Zn^{2+}$ binding.

1276 MST was used to experimentally measure $Zn^{2+}$ binding affinity at each site (panels A, B and C).
1277 These data were combined with a thermodynamic model, represented in panel H, with
1278 parameters derived either from CpHMD (panels D and E) or MST inference (panels F and G).
1279 (A) For MST studies of site A, the D70A/D287A/H263A construct was used with $Zn^{2+}$ buffered
1280 either with NTA (pH 7.0 and 7.4) or with citrate (pH 5.6, 6.0 and 6.5). Curves represent the law
1281 of mass action with $K_d$ values listed in Table 2. The relatively poor fit at pH 7.4 may reflect the
1282 fact that the $K_d$ (1 nM) is lower than the minimum protein concentration (8 nM) supported by the
1283 assay, thus moving the system from the binding to the titration regime (Jarmoskaite et al.,
1284 2020). (B). For MST studies of site B, the D51A/D287A/H263A construct was used and $Zn^{2+}$
1285 was buffered with citrate. (C) For MST studies of site C, the D51A/D70A construct was used
1286 and $Zn^{2+}$ was buffered with NTA at pH 7 or with citrate at the other pH's. (D,E) Curves represent
1287 predictions of a thermodynamic model with $pK_a$ values for either site A residues (Asp47, Asp51,
1288 His153, Asp157) or site B residues (D70, H73, H77) taken from CpHMD simulations. These $pK_a$
1289 values are listed in Table 4 and the distributions of protonation states are shown in Suppl. Figs.
1290 10 and 11. Symbols represent experimental MST data as in A and illustrate a poor fit using
1291 these parameters. Thermodynamic modeling was not possible for site C because of instability of
1292 the CTD in CpHMD simulations in the absence of $Zn^{2+}$. (F,G). Curves represent predictions of
1293 the MST inference algorithm with corresponding $pK_a$ values listed in Table 4. Again, symbols
1294 represent experimental MST data and show the excellent fit using these refined parameters. (H)
1295 Schematic representation of the microscopic thermodynamic model for site A. Titratable
1296 residues (D47, D51, D159, H155) are represented either as black squares for the protonated
1297 state, or white squares for the deprotonated state. Binding of one $Zn^{2+}$ ion to the site is indicated
1298 by a filled magenta circle. Transitions are only possible between states connected by lines
1299 (protonation/deprotonation) or corresponding states connected by double-sided arrows ($Zn^{2+}$
1300 binding/release). An analogous model for site B comprised D70, H73 and H77 (not depicted).

1301

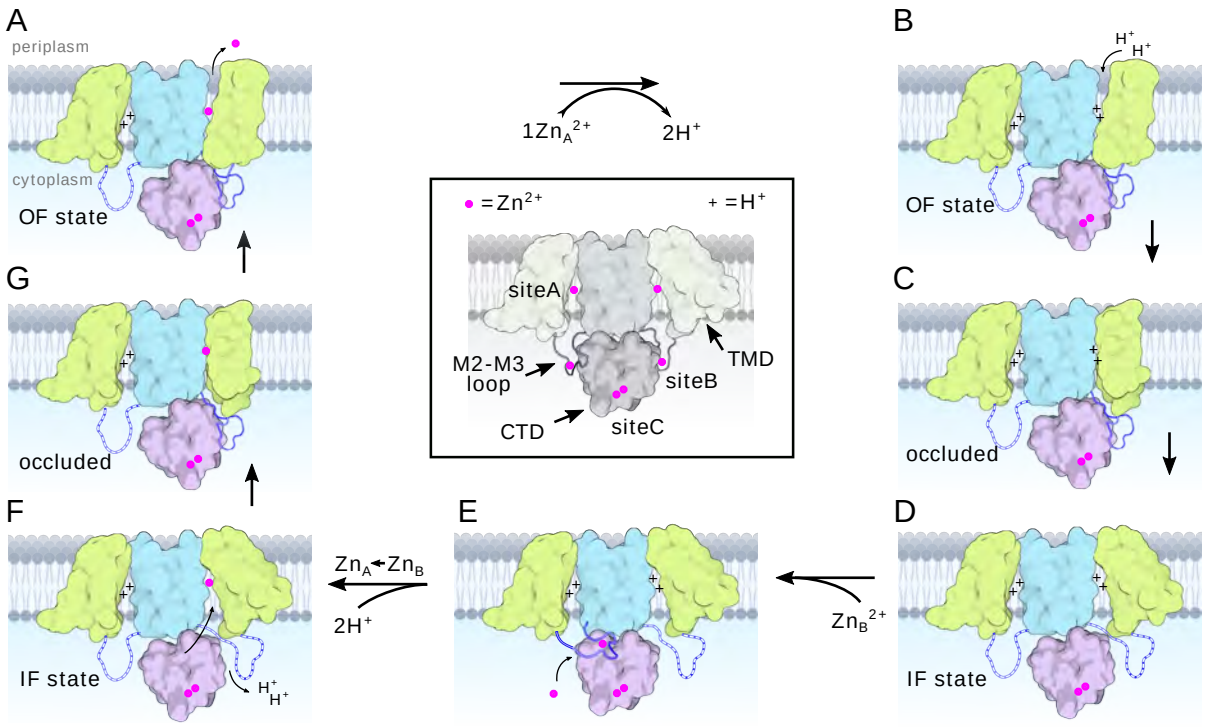
A
periplasm
cytoplasm
OF state
B
OF state
C
occluded
D
IF state
E
F
IF state
G
occluded
1Zn$_A^{2+}$
2H$^+$
= Zn$^{2+}$
+ = H$^+$
siteA
M2-M3 loop
TMD
siteB
CTD
siteC
Zn$_A$ ← Zn$_B$
2H$^+$
Zn$_B^{2+}$

Figure 5

1302 Figure 5. Transport cycle for YiiP.

1303 According to the alternating access paradigm, YiiP toggles between the OF and IF states via an
1304 intermediate occluded state. We assume that these changes occur independently in each
1305 protomer based on asymmetry seen in structures of soYiiP and Znt8 (Xue et al., 2020). Thus,
1306 our model depicts changes in the right-hand protomer while the left-hand protomer remains in a
1307 resting IF state. Although these intermediate states are informed by current and past structural
1308 work, they do not precisely conform to solved structures but represent hypothetical states that
1309 we believe to exist under physiological conditions. (A) $Zn^{2+}$ is released to the periplasm. The
1310 TM2/TM3 loop is depicted interacting with the CTD in a $Zn^{2+}$-free, extended conformation, as
1311 seen in our D70A_asym structure. (B) The release of $Zn^{2+}$ is promoted by the low pH of the
1312 periplasm and results in protonation of two residues in site A, or potentially three residues at
1313 lower pH. (C-D) The protonated form transitions to the IF state via an occluded state. In the IF
1314 state, the $Zn^{2+}$-free TM2/TM3 loop is released by the CTD and becomes disordered. (E) $Zn^{2+}$ is
1315 recruited to site B, inducing an ordered conformation of the TM2/TM3 loop that folds onto the
1316 CTD enabling interaction of Asp72 and Arg210. (F) $Zn^{2+}$ is transferred from a relatively low
1317 affinity site B to the much higher affinity site A via a negatively charged access channel, thus
1318 displacing two protons. (G) This transfer induces a $Zn^{2+}$-bound, occluded conformation in which
1319 the CTD tilts toward the occluded protomer and interacts with the TM2/TM3 loop in its $Zn^{2+}$-free,
1320 extended conformation. Features of the model are illustrated in the middle, boxed panel with
1321 desaturated colors. $Zn^{2+}$ ions are depicted as magenta spheres and protons with a "+". The CTD
1322 is pink with two $Zn^{2+}$ ions constitutively bound at site C. The scaffolding membrane helices (TM3
1323 and TM6) are blue and the transport domain (TM1,2,4,5) is yellow. The TM2/TM3 loop is blue
1324 and depicted with dashed lines in the disordered state. Created with biorender.com.

1325

# Tables

## Table 1. Structure determination of YiiP mutants

| **Data set** | WT | Site A D51A | Site B[1] D70A asymTMD | Site B[1] D70A symTMD | Site C D287A | Site C[2] D287A/ H263A |
|---|---|---|---|---|---|---|
| **Deposition** | | | | | | |
| PDB | 8F6E | 8F6F | 8F6H | 8F6I | 8F6J | 8F6K |
| EMDB | EMD-28881 | EMD-28882 | EMD-28883 | EMD-28884 | EMD-28885 | EMD-28886 |
| **Data collection and processing** | | | | | | |
| Magnification | 81,000 | 81,000 | 81,000 | 81,000 | 81,000 | 81,000 |
| Voltage (kV) | 300 | 300 | 300 | 300 | 300 | 300 |
| Electron exposure ($e^-$/Å$^2$) | 50 | 50 | 50 | 50 | 50 | 50 |
| Defocus range (μm) | 1.0-3.0 | 0.75-2.75 | 0.7-3.0 | 0.7-3.0 | 0.7-3.0 | 0.7-2.5 |
| Pixel size (Å) | 1.068 | 1.079 | 1.079 | 1.079 | 1.079 | 1.079 |
| Symmetry imposed | C2 | C2 | C1 | C1 | C2 | C2 |
| Initial particle images (no.) | 3,058,414 | 3,672,562 | 1,702,119 | 1,702,119 | 1,664,097 | 2,982,749 |
| Final particle images (no.) | 536,206 | 196,484 | 188,414 | 182,413 | 252,599 | 300,844 |
| Map resolution | 3.78 | 3.63 | 3.93 | 4.03 | 3.68 | 3.46 |
| FSC threshold (Å) | 0.143 | 0.143 | 0.143 | 0.143 | 0.143 | 0.143 |
| B factor (Å$^2$) | 200.5 | 151.0 | 146.1 | 126.0 | 150.9 | 135.2 |
| Resolution range (Å) | 3.0-5.5 | 3.0-5.2 | 3.4-5.8 | 3.4-6.9 | 3.0-5.5 | 3.0-5.2 |
| **Model Refinement** | | | | | | |
| Model composition | | | | | | |
| Non-hydrogen atoms | 10478 | 10348 | 10421 | 10377 | 10472 | 8714 |
| Protein residues | 1366 | 1344 | 1358 | 1351 | 1366 | 1132 |
| Ligands | 8 | 6 | 6 | 6 | 8 | 4 |
| RMS deviations | | | | | | |
| Bond lengths (Å) | 0.003 | 0.003 | 0.002 | 0.002 | 0.003 | 0.002 |
| Bond angles (°) | 0.557 | 0.535 | 0.509 | 0.517 | 0.536 | 0.499 |
| Validation | | | | | | |
| MolProbity score | 1.70 | 1.68 | 1.72 | 1.75 | 1.77 | 1.96 |
| Clashscore | 5.44 | 6.31 | 5.78 | 7.11 | 6.37 | 10.28 |
| Rotamer outliers (%) | 0.00 | 0.09 | 0.00 | 0.00 | 0.00 | 0.00 |
| CaBLAM outliers (%) | 2.66 | 3.05 | 2.60 | 3.40 | 3.64 | 4.21 |
| Rama-Z score | -0.77 | -0.37 | -0.05 | 0.20 | -0.50 | -0.45 |
| Ramachandran plot | | | | | | |
| Favored (%) | 94.19 | 95.27 | 93.99 | 94.86 | 93.59 | 93.51 |
| Allowed (%) | 5.44 | 4.57 | 5.86 | 4.99 | 6.04 | 5.96 |
| Disallowed (%) | 0.37 | 0.15 | 0.15 | 0.15 | 0.37 | 0.53 |
| Model vs. Data CC (mask) | 0.75 | 0.83 | 0.79 | 0.80 | 0.81 | 0.73 |

[1] Both D70A structures arose from the same set of micrographs and initial particle picks.
[2] Fab molecules were not included for the refinement of D287A/H263A due to poor density in this region of the map

Table 2. Binding affinity for individual $Zn^{2+}$ sites measured by MST* or deduced by the MST inference algorithm[§]

| | site A D70A/ D287A/H263A (μM) | site A/C D70A/D287A (μM) | site B D51A/ D287A/H263A (μM) | site C D51A/D70A (μM) | site C1 D51A/ D70A/H263A (μM) | site C2 D51A/ D70A/H234A (μM) |
|---|---|---|---|---|---|---|
| pH 5.6 | 302 ± 107 (149) | | 27.1 ± 2.8 (19.5) | 8.10 ± 1.55 | | |
| pH 6.0 | 6.11 ± 1.32 (10.8) | 6.30 ± 1.94 | 5.54 ± 2.0 (5.38) | 0.692 ± 0.28 | | |
| pH 6.5 | 0.654 ± 0.173 (0.503) | | 5.73 ± 1.75 (1.36) | 0.088 ± 0.032 | | |
| pH 7.0 | 0.0163 ± 0.0041 (0.0325) | 0.0012 ± 0.0018 | 1.18 ± 0.6 (0.503) | 0.033 ± 0.0087 | 0.153 ± 0.048 | 0.223 ± 0.039 |
| pH 7.4 | 0.001 ± 0.001 (0.0048) | | | | | |

* Values correspond to $K_d$ as determined by applying the law of mass action to the data.
[§] Values deduced by MST inference are shown in parentheses

Table 3. Binding affinity and Hill coefficients derived from MST data*

| | site A D70A/ D287A/H263A (μM) | site B D51A /D287A/H263A (μM) | site C D51A/D70A (μM) | site C1 D51A/ D70A/H263A (μM) | site C2 D51A /D70A/H234A (μM) |
|---|---|---|---|---|---|
| pH 5.6 | 1490 ± 2460 n=0.46 | 28.4 ± 3.54 n=0.94 | 7.50 ± 2.20 n=0.9 | | |
| pH 6.0 | 6.34 ± 1.67 n=0.81 | 5.68 ± 1.57 n=1.60 | 1.39 ± 0.382 n=0.78 | | |
| pH 6.5 | 0.622 ± 0.198 n=0.54 | 27.9 ± 34.3 n=0.38 | 0.133 ± 0.0359 n=0.66 | | |
| pH 7.0 | 0.0247 ± 0.0057 n=1.0 | 4.23 ± 13.0 n=0.45 | 0.0486 ± 0.0038 n=2.9 | 0.116 ± 0.0119 n=2.96 | 0.212 ± 0.0328 n=1.2 |
| pH 7.4 | 0.0039 ± 0.0009 n=0.56 | | | | |

* Values correspond to $EC_{50}$ and the Hill coefficient (n) as determined by fitting the Hill equation to the data.

Table 4. p$K_a$ values of residues determined by CpHMD simulations (Hill-Langmuir) and MST inference

| | | CpHMD (Hill-Langmuir) | MST inference |
|---|---|---|---|
| Site A | Asp47 | 3.84 ± 0.18 | -0.20 ± 0.51 |
| | Asp51 | 2.92 ± 0.12 | 6.51 ± 0.21 |
| | His155 | 7.97 ± 0.15 | 7.82 ± 0.15 |
| | Asp159 | 4.87 ± 0.18 | 7.83 ± 0.15 |
| Site B | Asp70 | 2.06 ± 0.46 | 1.12 ± 0.57 |
| | His73* | 8.08 ± 0.46 | 12.37 ± 0.61* |
| | His77* | 8.12 ± 0.13 | 5.26 ± 0.47* |

* Titration curves for His73 and His77 from the MST inference model cannot be fit individually with a simple Hill equation (c.f. Suppl. Figs. 11e & f). We therefore consider these two residues as a coupled system with two effective p$K_a$ values as shown.

Table 5. MD simulations

| Simulation | length | N of replicas | Total simulation time | software |
|---|---|---|---|---|
| Fixed charge *apo** | 1000 ns | 3 | 3000 ns | GROMACS |
| Fixed charge *holo** | 1000 ns | 3 | 3000 ns | GROMACS |
| Fixed charge *empty site B* | 1000 ns | 6 | 6000 ns | GROMACS |
| Fixed charge D72A | 1000 ns | 3 | 3000 ns | GROMACS |
| CpHMD apo | 12 ns | 30 (pHREX) | 360 ns | CHARMM |

"Fixed charge" simulations were repeated three times. The CpHMD simulations were performed as coupled pH-replica exchange simulations.

*Simulations for apo and holo YiiP were taken from our previous work (Lopez-Redondo et al., 2021)

Table 6. MST convergence criteria

| Target | Binding site | RMSD cutoff |
|---|---|---|
| CpHMD microstate probability distributions | Site A | 0.0382 |
| CpHMD microstate probability distributions | Site B | 0.0447 |
| MST bound fraction | Site A | 0.0760 |
| MST bound fraction | Site B | 0.0995 |